Chapter 6 : Results and Discussion

6.1 Background

The tests performed as part of this research were the second attempt to demonstrate the Virginia Tech DGV system could perform as a viable flow velocity measurement system. As was the case in the first attempt to verify the performance of the VT DGV system, this attempt was marginally successful. As was mentioned in Chapter 5, the acquisition and reduction of iodine cell calibrations, calibration wheel velocity data, and flow field velocity data were complicated by hardware problems with the Nd:YAG laser and the digital cameras. Because of these problems, a disproportionately large number of iodine cell calibrations were acquired before an attempt was made to acquire velocity images. Also as a result of these problems, two sets of calibration wheel data were acquired only to find that the data images were not usable because the iodine absorption features had moved after the iodine cell calibration scan used to calculate the frequency calibration function was completed. A method was developed to adjust the optical frequency of the laser so the desired unshifted mean transmission ratio was achieved. While the performance of the system was less than desirable, the system was capable of detecting changes in the optical frequency of light due to the Doppler effect.

6.2 Iodine Cell Calibration Results

A series of iodine cell calibrations were performed prior to attempting to acquire velocity data images from the calibration wheel or in the wake of the 6:1 prolate spheroid. The procedure followed in

acquiring these calibrations was to first acquire a scan over a large range of offset voltages to determine the location of the iodine absorption features of interest and then acquire a scan over a smaller range of voltages to obtain a high resolution plot of the absorption feature to be used to acquire velocity data. The implementation of this procedure was complicated by the problems with the Nd:YAG laser and the digital cameras. Several attempts were required to obtain a successful large range scan and short range scan back to back, because the iodine absorption features frequently moved during the scan or between scans. The procedure described in section 4.2 was used to reduce the images acquired during each calibration. Figure 6.1 is a plot of five iodine cell calibration scans illustrating the movement of the iodine absorption features between scans. The mean transmission ratios acquired by camera module 2 during a series of iodine cell calibrations are shown in this figure.

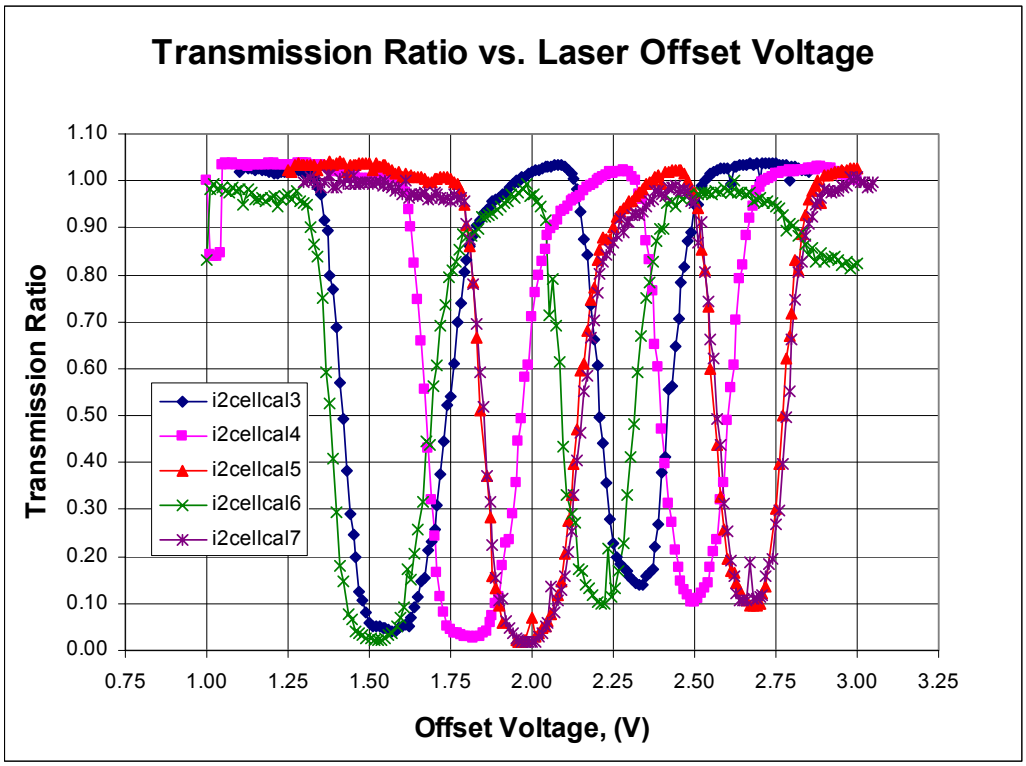

Figure 6.1: Movement of iodine absorption features between iodine cell calibration scans

Chapter 5 discusses some of the attempts made to correct this problem with the Nd:YAG laser. The laser and camera problems eventually led to attempts to decrease the length of time needed to acquire an iodine cell calibration. The decision was made to trade calibration resolution for time, so the number of calibration images acquired over a given voltage was significantly decreased. This allowed a calibration over a large voltage range to be acquired in less time than was required when

the rule of thumb of 50 images for every 0.5 volts was employed. Eventually, roughly 25 to 30 images for every 0.5 volts was used as a rule of thumb for acquiring a calibration. This allowed the correction images and calibration to be acquired without having to turn off the cameras to prevent ice crystals from forming in camera 3. While this did not eliminate the problem with the absorption features moving, iodine cell calibrations could be acquired faster and improved the chances of locating the desired absorption feature in time to acquire velocity images. Figure 6.2 is a plot showing mean transmission ratios acquired by camera module 2 during a later series of iodine cell

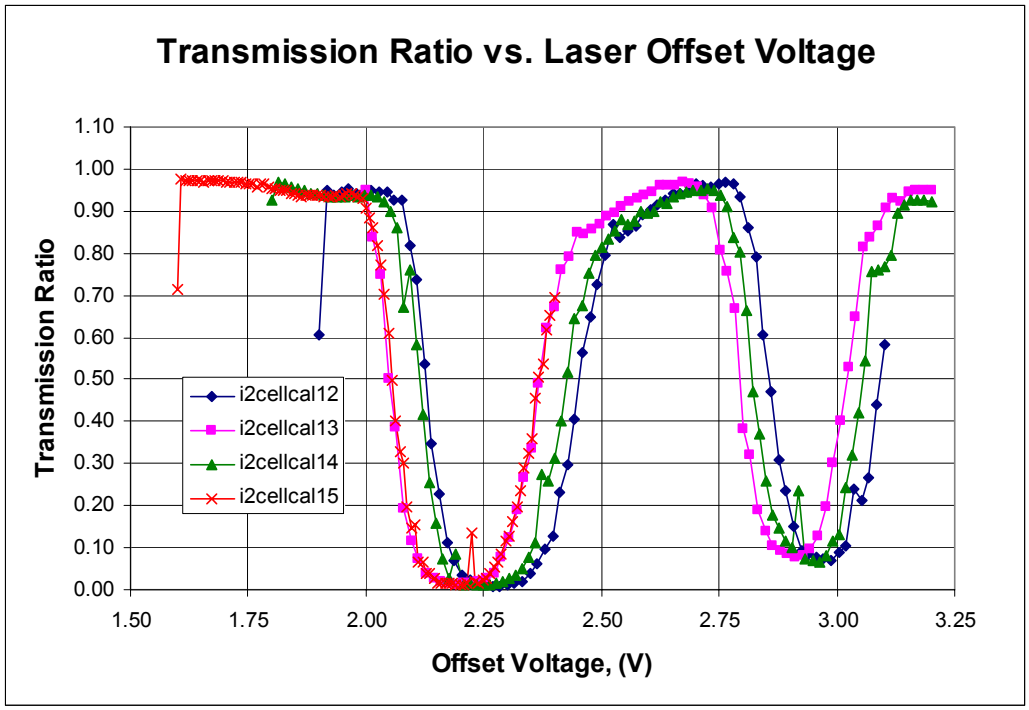

Figure 6.2: Lower resolution iodine cell calibrations.

calibrations. The calibration designated i2cellcal15 in this figure was acquired just prior to the third attempt to acquire velocity data images of the calibration wheel. This calibration was used to calculate the frequency calibration functions used to reduce the acquired calibration wheel velocity images. Figure 6.3 shows two of the iodine cell calibrations acquired just prior to the attempt to acquire velocity data in the wake of the 6:1 prolate spheroid. If velocity data images had been successfully acquired in the wake of the prolate spheroid, the calibration designated i2cellcal18 in figure 6.3 would have been used to calculate the frequency calibration functions used to reduce these velocity images.

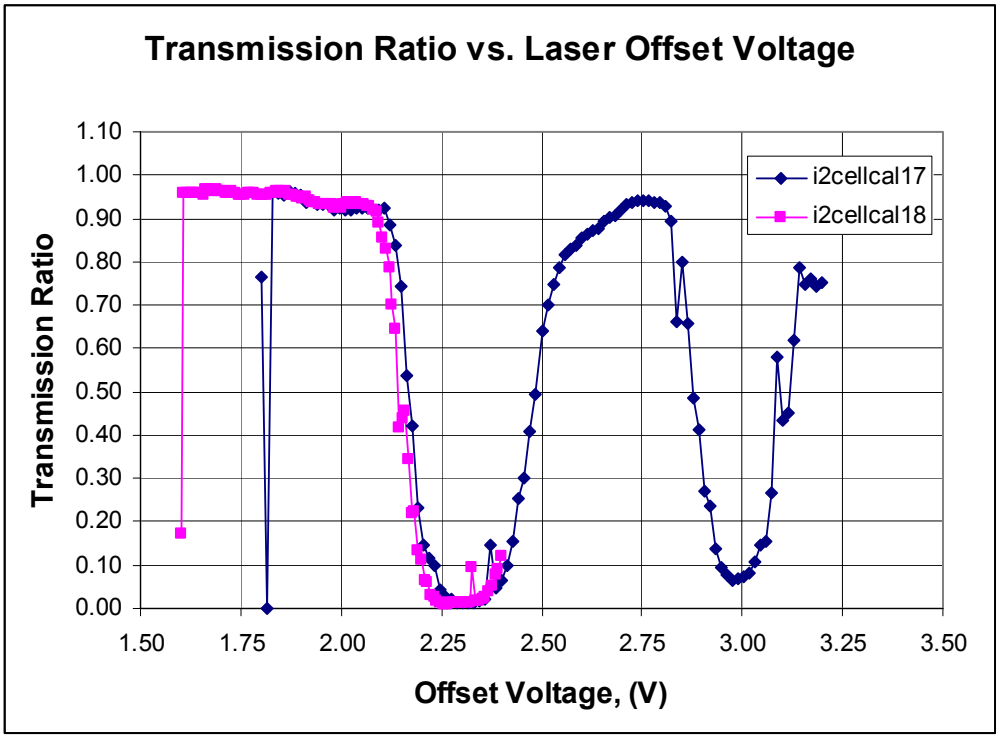

Figure 6.3: Iodine cell calibrations acquired prior to attempting to acquire velocity data images in the wake of the 6:1 prolate spheroid.

6.3 Background for Calibration Wheel Results

As was mentioned in section 6.1, three attempts were made to acquire velocity data from the calibration wheel. Only the images acquired in the third attempt were usable. During the first attempt to acquire calibration wheel data, the absorption features moved so the velocity images were acquired at an optical frequency where the transmission ratio was near its maximum value for the absorption feature being used. In the second attempt, the iodine absorption feature moved so the velocity images were acquired near the minimum transmission ratio for the absorption feature being used. As figures 6.1 and 6.2 demonstrate, there were plateaus and valleys where the maximum and minimum transmission ratios occurred. Data acquired near the maximum or minimum transmission ratio for a particular absorption feature are unreliable because the transmission ratio is not very sensitive to changes in optical frequency in these regions. Ideally, velocity data should be acquired midway between the maximum and minimum transmission ratios of a given absorption feature.

While no solution to the problem of the absorption features moving was found, a method for adjusting the offset voltage was developed so the transmission ratios measured by the camera modules were roughly midway between the maximum and minimum transmission ratios, for the absorption feature. In this method the offset voltage was set to the value believed to be where the mid

point of the absorption feature was located. Next, an image was acquired of the motionless calibration wheel or a solid white target, and the mean transmission ratio for each camera module was calculated. After the transmission ratio for each camera module was calculated the offset voltage was adjusted and the procedure repeated until the mean transmission ratios from each camera module were roughly halfway between the maximum and minimum transmission ratios for the absorption feature. There were, however, two major problems with this technique. First, there was no guarantee that the desired absorption feature was in fact the absorption feature being used to set the transmission ratios. Second, this procedure required time to perform. If more than 10 to 15 minutes was required to set the offset voltage so the desired transmission ratio was achieved, the problem with one of the digital cameras forming ice crystals on the CCD array would interfere with the acquisition of velocity data.

6.4 Calibration Wheel Reduction Settings

Before the calibration wheel data was reduced, the procedures described in 3.5, 4.3, 4.4, and 4.5 were performed to calculate values needed for the data reduction procedure. These values included the Euler angles for each of the camera modules, frequency calibration function for each camera module, reference mean transmission ratio for each camera module, reference value for the laser reference transmission ratio, and the unit vector in the direction of laser propagation. Each of these values will be discussed in the subsections below.

6.4.1 Euler Angles for Camera Modules

The procedure from 3.5 was used to determine the Euler angles for each of the camera module. The rotation matrices and Euler angles output by the camera calibration toolbox were as follows:

Camera Module 1 (Above test section):

$$R_1 = \begin{bmatrix} -0.021466 & 0.999742 & -0.007396 \\ 0.846103 & 0.022107 & 0.532561 \\ 0.532587 & 0.005174 & -0.846359 \end{bmatrix} \Rightarrow \begin{Bmatrix} 147.8204^\circ \\ 0.4238^\circ \\ 91.2306^\circ \end{Bmatrix} \tag{41}$$

Camera Module 2 (Port side of test section):

$$R_2 = \begin{bmatrix} 0.022546 & 0.915402 & 0.401909 \\ 0.992868 & -0.067577 & 0.098220 \\ 0.117071 & 0.396828 & -0.910397 \end{bmatrix} \Rightarrow \begin{Bmatrix} 173.8423^\circ \\ -23.6976^\circ \\ 91.4109^\circ \end{Bmatrix} \tag{42}$$

Camera Module 3 (Starboard side of test section):

$$R_3 = \begin{bmatrix} -0.013766 & 0.929243 & -0.369213 \\ 0.846103 & 0.022107 & -0.058087 \\ 0.532587 & 0.005174 & 0.927528 \end{bmatrix} \Rightarrow \begin{Bmatrix} 183.5835^\circ \\ 21.6671^\circ \\ 90.8481^\circ \end{Bmatrix} \tag{43}$$

It should be noted that problems were experienced with determining the Euler angles for camera module 2. When the Euler angles calculated from the rotation matrix output by the calibration toolbox were used to calculate a rotation matrix, the some of the terms in the calculated matrix did not match the values in the matrix output by the toolbox. The maximum deviation between the values in the calculated matrix and the values in the matrix output by the toolbox was 0.049. Attempts were made to correct for this difference by changing the images used to calculate the rotation matrix but these attempts had no significant effect on the rotation matrix output by the calibration toolbox. The signs and magnitudes of the Euler angles calculated from the rotation matrix output by the toolbox matched estimates made of the Euler angles made while the VT DGV system was in the wind tunnel so these values were used in the data reduction. The additional rotations described in section 3.5 were performed on the Euler angles calculated from the rotation matrices output by the camera calibration toolbox. The Euler angles input into the data reduction were as follows:

Camera Module 1 (Above test section):

$$\theta_1 = \begin{Bmatrix} 32.1796^\circ \\ 0.4238^\circ \\ -1.2306^\circ \end{Bmatrix} \tag{44}$$

Camera Module 2 (Port side of test section):

$$\theta_2 = \begin{Bmatrix} 6.1577^\circ \\ -23.6976^\circ \\ -1.4109^\circ \end{Bmatrix} \tag{45}$$

Camera Module 3 (Starboard side of test section):

$$\theta_3 = \begin{Bmatrix} -3.5835 \\ 21.6671 \\ -0.8481 \end{Bmatrix} \tag{46}$$

6.4.2 Frequency Calibration Functions

The procedure described in section 4.3 was used to calculate the frequency calibration function for each camera module. Figure 6.4 is a plot of the white card corrected iodine cell calibration used to calculate the functions. Notice that the calibrations from camera modules 1 and 2 overlay each other nicely but the calibration from camera module 3 is significantly different from the

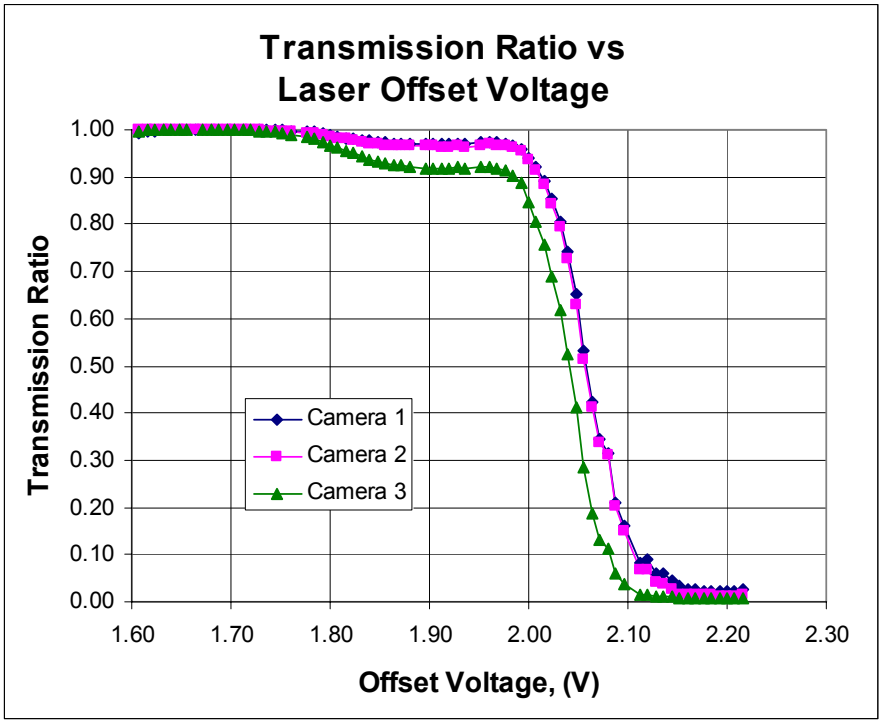

Figure 6.4 Iodine cell calibration

other two. This was the case for all of the iodine cell calibrations performed in the Virginia Tech Stability Wind Tunnel. There are several possible explanations for this difference. The first possible explanation for the difference in the calibrations from camera modules 1 and 2 and that of camera module 3 is that the iodine cell in camera module 3 could have been filled at a temperature different from the temperature at which the cells in camera modules 1 and 2 were filled. Figure 6.5 shows how filling temperature affects the absorption properties of an iodine cell. While the plot in figure 6.5 shows a very similar trend to that observed in figure 6.4, if the iodine cell in camera module 3 was in fact filled at a different temperature this problem would have been noticed in laboratory tests of the

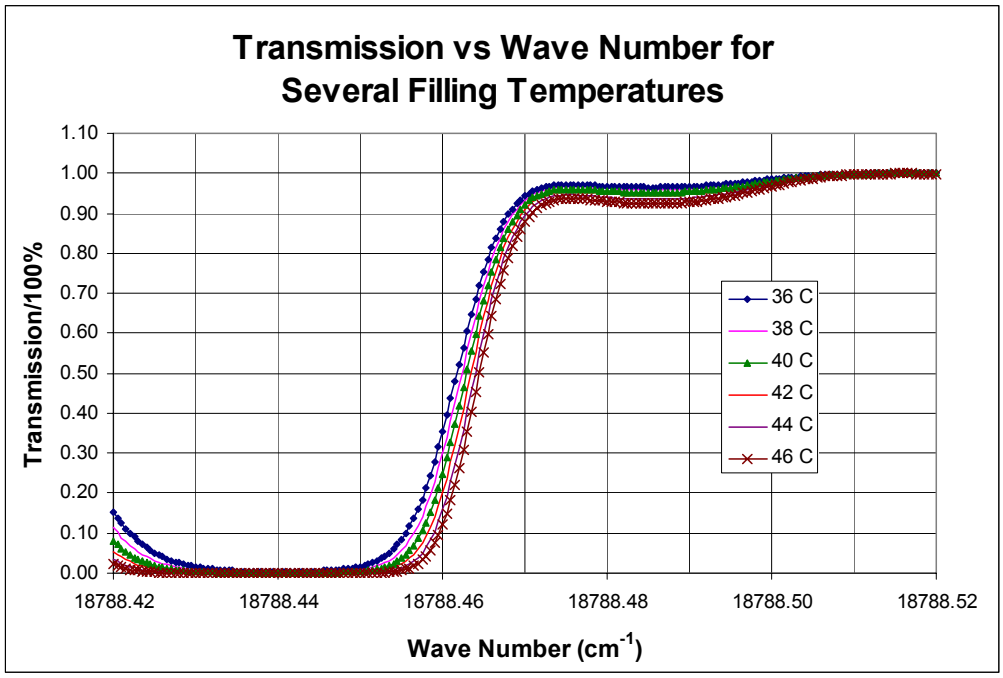

Figure 6.5: Effects of filling temperature on iodine cell absorption properties

system prior to testing the system in the wind tunnel. Another possible explanation is that camera module 3 viewed the data plane through the same Plexiglas panel through which the laser was fired. It is possible that the laser light passing through the Plexiglas panel could have had this effect on the calibration results obtained by camera module 3. The significant difference in the iodine cell calibration results made it necessary to have a separate frequency calibration function for each camera module. This would be desirable even if there wasn't a significant difference between the calibration results of the camera modules, because there are usually small differences in the calibration results obtained by each of the camera modules. The procedure described in section 4.3 was used to calculate the 5th order frequency calibration functions and to produce the plot shown in figure 6.6. The calculated frequency calibration functions were as follows:

Camera Module 1(Above test section):

$$y = 0.0371x^5 - 0.0567x^4 + 0.0540x^3 - 0.0501x^2 + 0.0364x + 18788 \qquad (47)$$

Camera Module 2 (Port side of test section):

$$y = 0.0046x^5 + 0.0449x^4 - 0.0681x^3 + 0.0195x^2 + 0.0018x + 18788 \qquad (48)$$

Camera Module 3 (Starboard side of test section):

$$y = 0.1889x^5 - 0.4897x^4 + 0.5066x^3 - 0.2509x^2 + 0.0676x + 18788 \qquad (49)$$

where y is the optical frequency, in the form of the wave number, and x is the transmission ratio. The coefficients for these functions were input into the dialog box shown in figure 4.4.

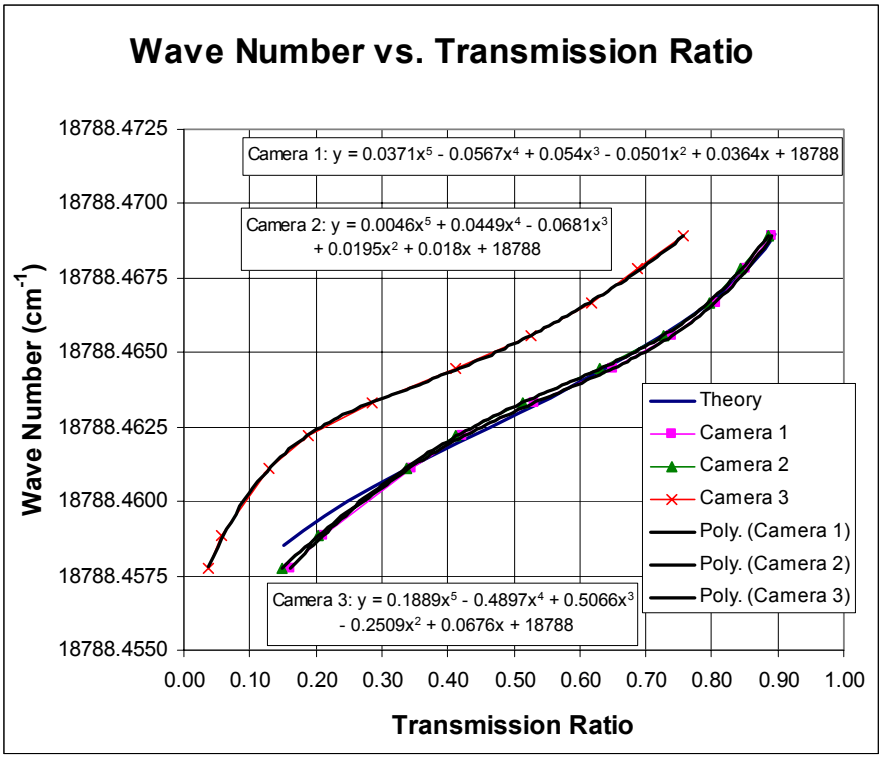

Figure 6.6: Plot of scaled iodine cell calibration results, theoretical absorption profile, and trend lines from frequency calibration functions.

6.4.3 Reference Transmission Ratios

The procedures described in sections 4.4.3, 4.5.3, and 4.5.5 were used to calculate the reference value for the laser reference transmission ratio and the reference transmission ratio for the each camera module. Camera module 3 was used to monitor variations in the optical frequency of the pulses output by the Nd:YAG laser. The reference value for the laser reference transmission ratio was 0.201773. The reference transmission ratio for camera module 1 was 0.474961. The reference transmission ratio for camera module 2 was 0.468240. The reference transmission ratio for camera module 3 was 0.218878, significantly less than the reference transmission ratios from camera modules 1 and 2. The difference in the reference value for the laser reference transmission ratio and reference transmission ratio from camera module 3 compared to those calculated for camera modules

1 and 2 was expected. This difference occurred for the same reasons the iodine cell calibrations acquired by camera module 3 were significantly different from those acquired by camera modules 1 and 2.

6.4.4 Laser Propagation Vector

There was some question about the direction of the laser propagation unit vector used to reduce the calibration wheel velocity images. It was known that for the cases where DGV data was acquired in a flow field, this unit vector was in the same plane as the data plane. Should this also be the case for the calibration wheel data, even though the laser was not being used to produce a sheet of laser light in the same plane as the data plane? Average images were calculated from the images acquired of the moving calibration wheel. These average images were used to reduce the calibration wheel images using two substantially different laser propagation vectors. The first vector was in the same plane as the data plane. The second vector was an estimate of the true laser propagation unit vector. This estimate was based on the Euler angles calculated for camera module 3. The orientation of this camera module was close to the direction the laser was fired to produce the cone of laser light used to illuminate the calibration wheel. Ideally, the reduced velocities measured in the z direction should be zero since the calibration wheel rotated in the x-y plane of the coordinate frame attached to the data plane. The velocities measured in the z direction were inspected for the two different laser propagation vectors to see if one approached the ideal condition where Vz = 0. Figure 6.7 is a contour plot of velocity in the z direction for the case where the laser propagation vector was taken to be in the data plane. Figure 6.8 is a plot of velocity in the z direction for the case where the estimate of the true laser propagation vector was used. By comparing the results shown in these plots, it was determined that the correct laser propagation unit vector to use in the data reduction procedure was the true laser propagation unit vector. The magnitudes of the velocities contained in the plot where the velocity vector was taken to be in the data plane are significantly higher than those in the plot where the real laser propagation vector was used. For the third set of calibration wheel data acquired in the Virginia Tech Stability Wind Tunnel the estimated laser propagation unit vector was:

$$l = \begin{Bmatrix} -0.5000 \\ -0.0604 \\ 0.8639 \end{Bmatrix} \tag{50}$$

In the future, a technique should be developed to accurately measure the laser propagation unit vector for both the cases where calibration wheel data is to be acquired and where velocity data in a flow field is to be acquired.

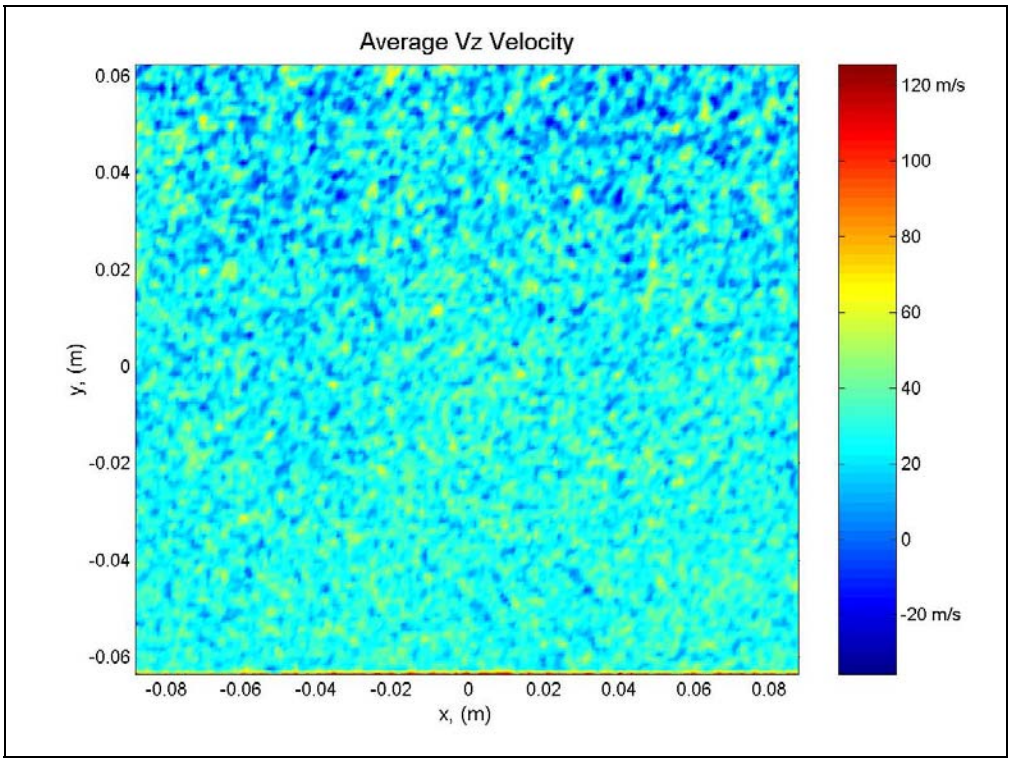

Figure 6.7: Contour plot of Vz velocity for the case where the laser propagation unit vector was taken to be in the same plane as the data plane

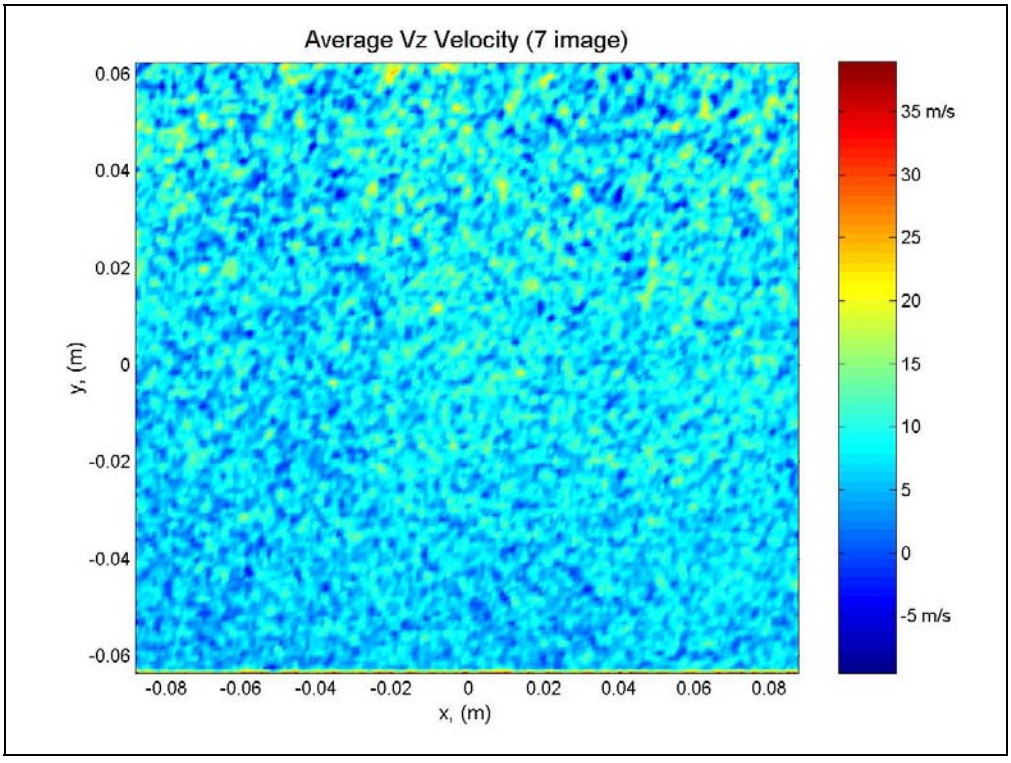

Figure 6.8: Contour plot of Vz velocity for the case where the laser propagation unit vector was taken to be the true laser propagation unit vector.

6.4.5 VT DGV setup used to acquire calibration wheel velocity data

Now that the Euler angles for each of the camera modules and the direction of the laser propagation vector have been determined, the complete setup of the VT DGV system used to acquire velocity data from the calibration wheel can be shown. This subsection contains a series of figures showing the setup of the VT DGV system used to acquire velocity data from the calibration wheel in the Virginia Tech Stability Wind Tunnel. This subsection also contains a figure showing the coordinate system attached to the data plane. This figure also shows the size and location of the data area on the calibration wheel. These figures are intended to clarify how the VT DGV system was setup in the Virginia Tech Stability Wind Tunnel during acquisition of velocity data from the calibration wheel as well as providing a visual reference for the discussion of the results from these tests.

Figure 6.9 is a drawing showing a plan view of the VT DGV setup in the Virginia Tech Stability Wind Tunnel with the Euler angles about the y axis for each of the camera modules and the laser propagation vector labeled. This figure also provides an estimate of the distance from the front end of the camera to the data plane for the camera modules on each side of the test section. Figure 6.10 is a drawing showing the setup of the VT DGV system from the control room. This figure shows the Euler angles about the x axis for the camera module in the control room, the camera module placed on top of the test section, and the laser propagation vector. This figure also provides an estimated distance from the front end of the camera to the data plane for the camera module placed on top of the test section. Figure 6.11 is a drawing showing the Euler angle about the x axis for the camera module mounted on the side of the test section opposite from the control room.

Figure 6.12 shows the coordinate system attached to the data plane. The origin of this coordinate system was placed at the center of the calibration wheel, with the z axis pointing down the shaft used to turn the calibration wheel. The origin of this coordinate system is also located at the center of the data area. The data area was a rectangle 0.1778 meters along the x axis by 0.127 meters along the y axis.

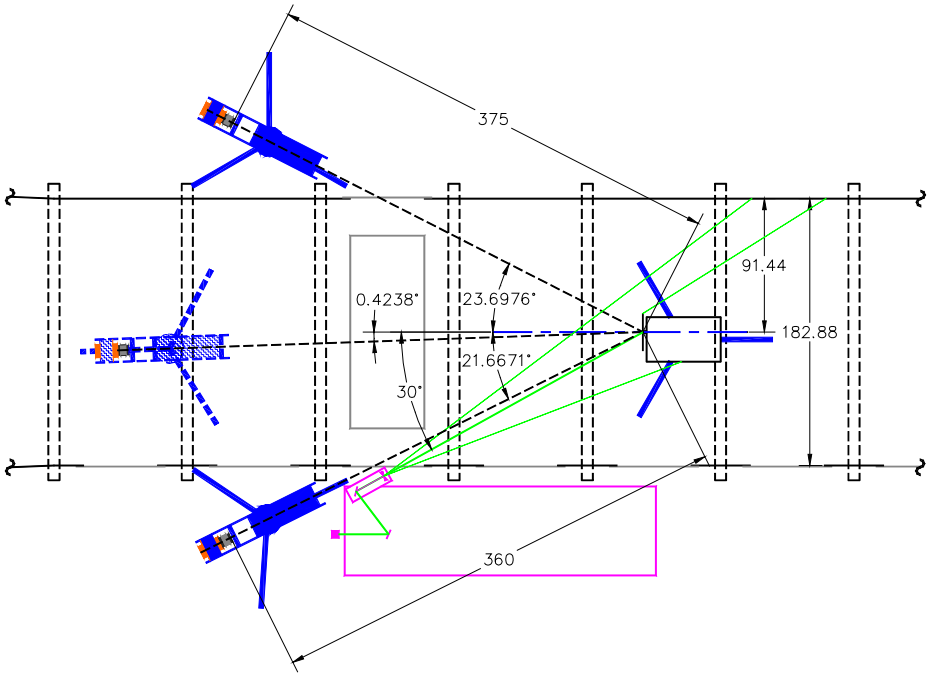

Figure 6.9: Dimensioned drawing showing the Euler angles about the y axis for each of the three camera modules and the distances from the front end of the camera to the data plane for the two camera modules mounted on the sides of the test section.

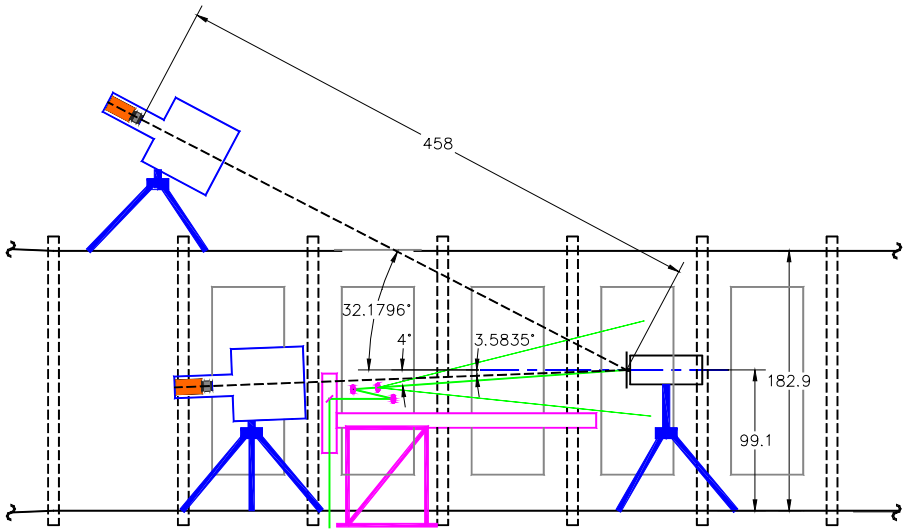

Figure 6.10: Dimensioned drawing showing the Euler angles about the x axis for the camera module in the control room and the camera module placed on top of the test section and the distance from the front end of the camera to the data plane for the camera module mounted on top of the test section.

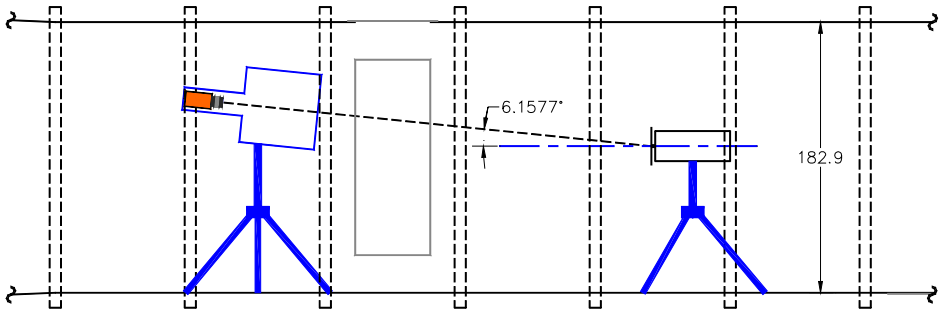

Figure 6.11: Dimensioned drawing showing the Euler angle about the x axis for the camera module placed on the side of the test section opposite to the control room.

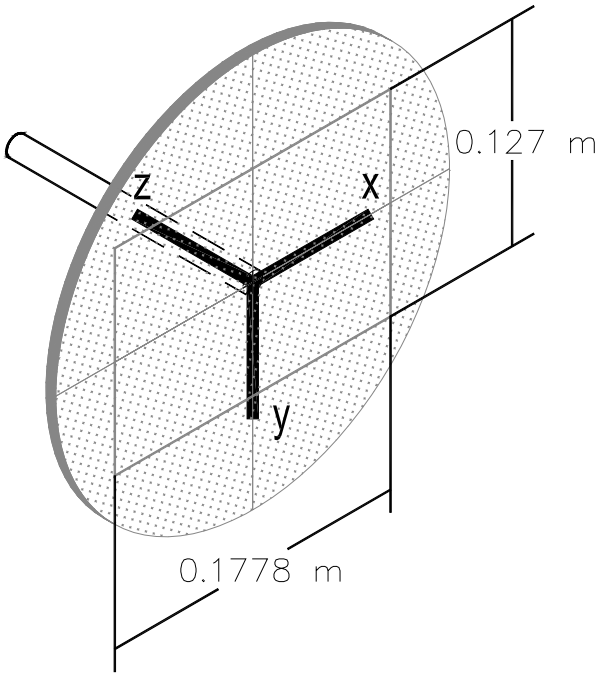

Figure 6.12: Drawing showing the orientation of the coordinate system attached to the data plane as well as the size and location of the data area.

6.5 Calibration Wheel Results

The third set of calibration wheel velocity images was acquired three days before the end of the tunnel entry scheduled to verify the performance of the VT DGV system. As mentioned previously, the two attempts made prior to this attempt were not successful because the optical frequency of the pulses output by the Nd:YAG laser had shifted out of the sensitivity range of the

iodine cell. The third set of 50 velocity images was acquired of the calibration wheel rotating at a commanded angular velocity of 50 revolutions per second. The procedure used to set the offset voltage to the laser had been adjusted to try to ensure that the optical frequency of the pulses emitted by the laser was such that the mean transmission ratio calculated by each of the camera modules was roughly 0.5. Because the light absorption properties of camera module 3 were significantly different from those of camera modules 1 and 2, this was not entirely possible. The offset voltage to the laser was set so that the mean transmission ratios measured by camera modules 1 and 2 were roughly 0.5 and this caused the mean transmission ratio measured by camera module 3 to be roughly 0.2. This decision meant that the sensitivity of camera module 3 to changes in the optical frequency due to the Doppler effect would be less than that of camera modules 1 and 2. This most likely had an effect on the quality of the data obtained from the VT DGV system in this test.

Another problem was discovered while the velocity images acquired of the calibration wheel were being reduced. An unusually large number of images were acquired while the laser was in a reset condition. Out of the 50 images acquired in this set of data, 32 images were acquired while the laser was reset. Images acquired while the laser was reset could not be used because the pulses emitted by the laser while it is reset are not the narrow bandwidth pulses needed to measure changes in optical frequency due to the Doppler effect. Only one image was acquired while the laser was reset during the 100 image iodine cell calibration acquired just prior to this attempt to acquire velocity images. The iodine cell calibrations acquired after this attempt did not have this problem either. Another interesting fact to note is that the Q-switch build up times for these images were no higher than the Q-switch build up times for the images acquired when the laser was not reset. Usually when the laser started to perform badly or when a bad pulse was fired, the Q-switch build up time would be noticeably higher than it was when the laser was performing correctly. The most likely explanation for the large number of images acquired while the laser was in a reset condition is that the calibration wheel was producing a RF signal that was picked up by the laser. Before the next attempt to acquire DGV data from the calibration wheel, this problem will have to be investigated further and a solution will have to be developed.

6.5.1 Velocity Components Calculated from the Angular Velocity

The output voltage from the motor controller was used to independently measure the angular velocity of the calibration wheel while each image was acquired. These voltages were used to calculate an average angular velocity for the images that were reduced. The average angular velocity calculated from the reduced images was 50.03 rev/s. This angular velocity was used to generate

contour plots of the x and y velocity components inside the data area. Figures 6.13 and 6.14 are contour plots showing the x and y components of velocity, respectively, calculated from the average angular velocity of the calibration wheel measured using the output voltage from the motor controller. A plot of the z component is not shown because the velocities in the z direction should all be zero.

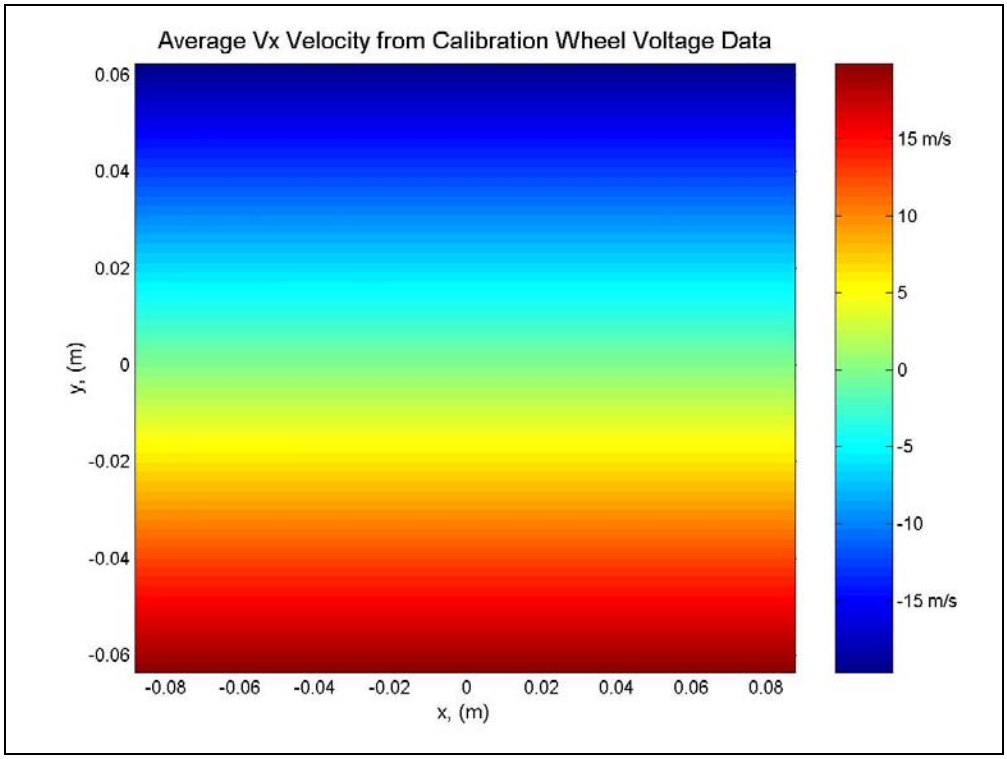

Figure 6.13: Contour plot of x velocity components calculated from average angular velocity measured using output voltage from motor controller

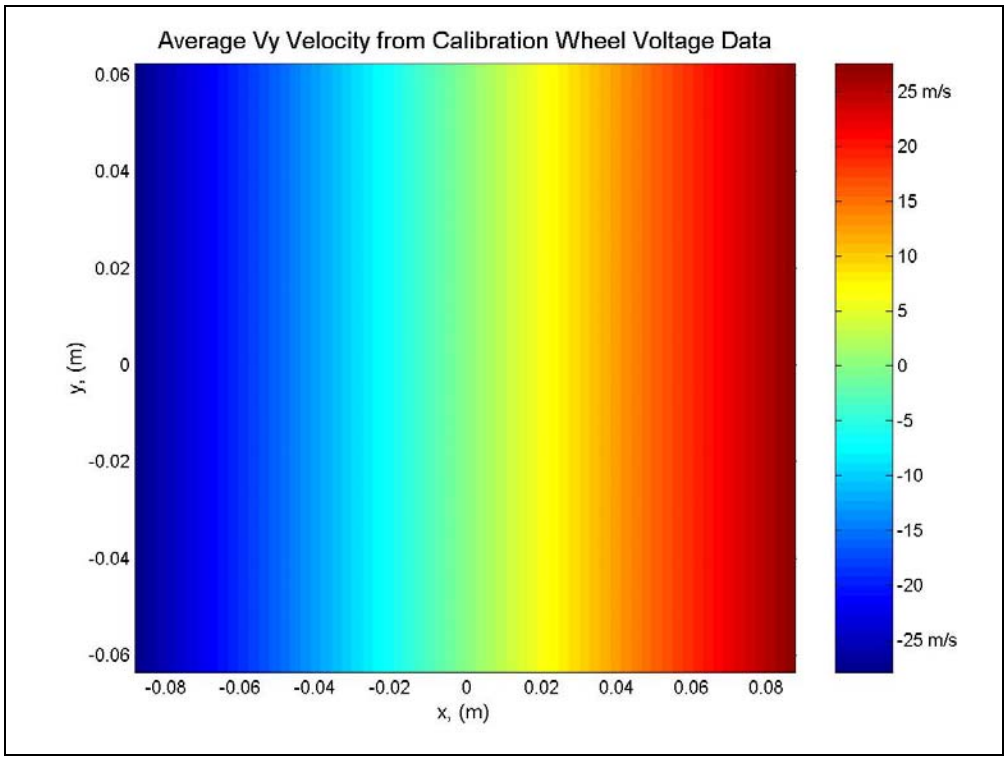

Figure 6.14: Contour plot of y velocity components calculated from average angular velocity measured using output voltage from motor controller

6.5.2 Sequence and Average Image Data Reduction

The sequence of velocity images acquired of the calibration wheel, except the images acquired while the laser was reset, were reduced using the transmission ratio and Q-switch build up time filtering options in the data reduction procedure, as described in section 4.5.3. Out of the remaining 18 images only seven sets of images passed through the transmission ratio and Q-switch build up time filtering to be reduced. These seven sets of images were used to calculate an average image for each camera module. These average images were also reduced and compared to the results of the sequence data reduction. Figures 6.15, 6.16 and 6.17 are contour plots of the average x, y and z components of velocity, respectively, calculated for the sequence of seven velocity images acquired from the calibration wheel. Figures 6.18, 6.19, and 6.20 are contour plots of the average x, y, and z components of velocity, respectively, calculated from the average images. Comparing the results from the image sequence data reduction and the average image data reduction to the plots of the x and y velocities calculated using the average angular velocity from the motor controller output voltage, the x and y velocity component plots from the data acquired by the VT DGV system show the same trends shown in figures 6.13 and 6.14. However, the magnitudes of the velocity components measured by the VT DGV system are higher than those calculated from the angular velocity of the

wheel. The most likely cause for this discrepancy is that the transmission ratios acquired by camera module 3 were closer to the minimum transmission ratio for the absorption feature being used to acquire velocity data, thus, the transmission ratios acquired by this camera module were not as sensitive to changes in optical frequency as were the transmission ratios acquired by camera modules 1 and 2. Given the problems with the optical frequency of the Nd:YAG laser drifting, as indicated by the movement of the iodine absorption features from calibration to calibration, it is also quite possible that the optical frequency of the pulses output by the Nd:YAG laser drifted such that the degradation in the sensitivity of camera module 3 was exaggerated.

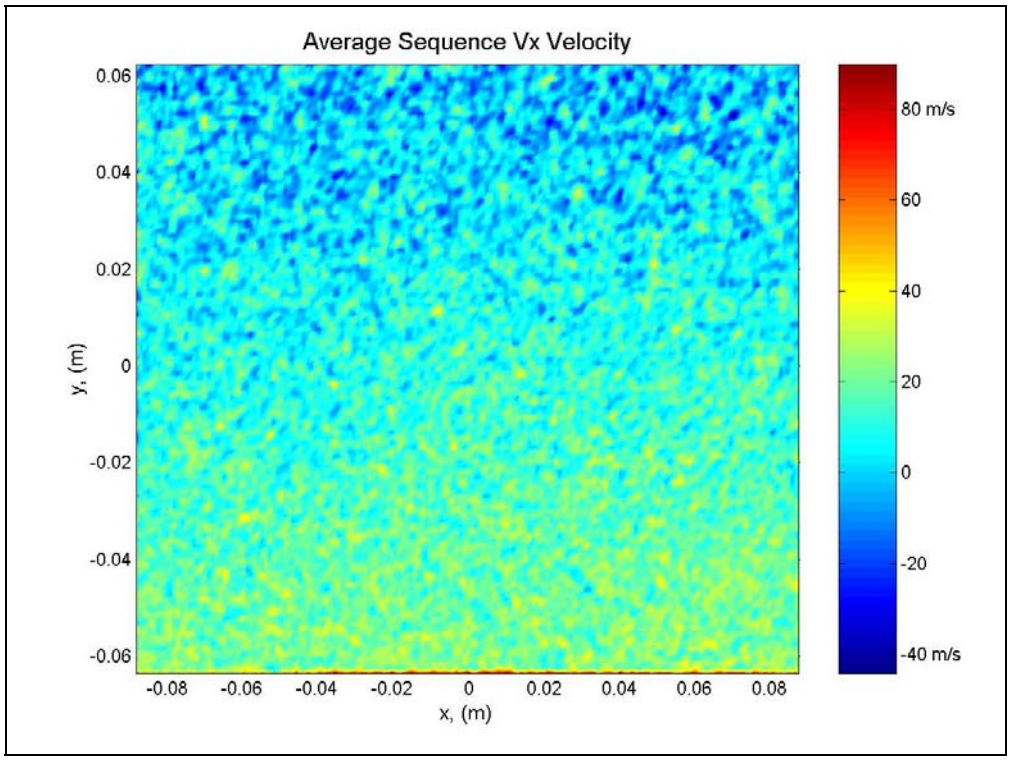

Figure 6.15: Contour plot of average x velocity components calculated by the image sequence data reduction procedure.

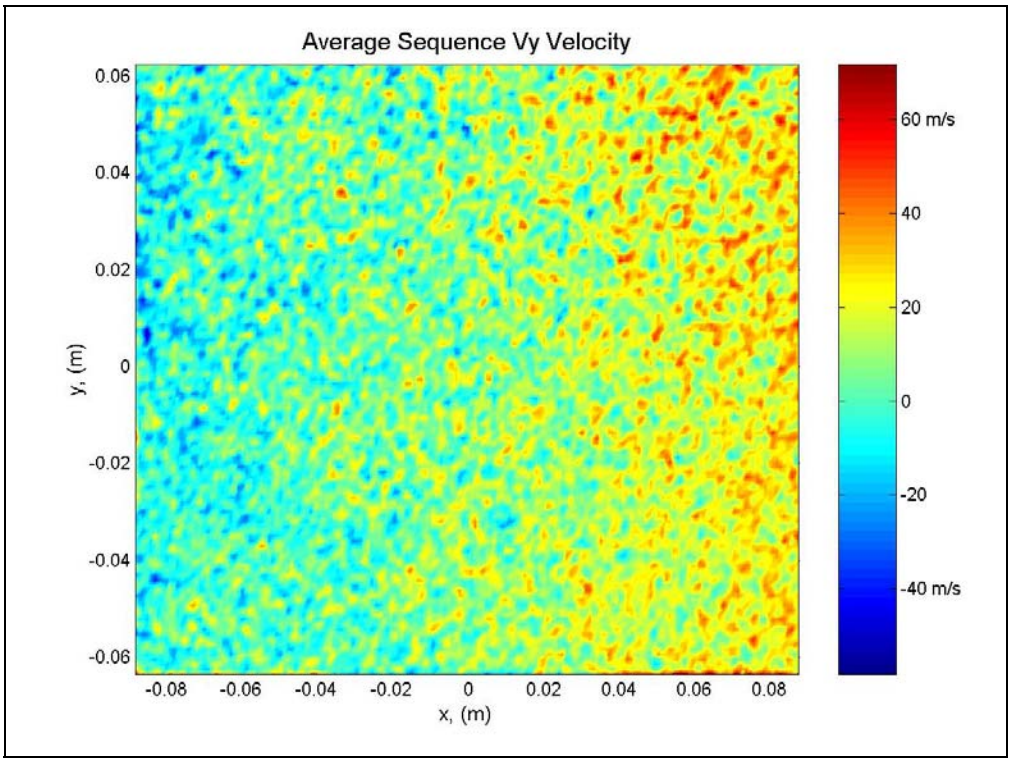

Figure 6.16: Contour plot of average y velocity components calculated by the image sequence data reduction procedure.

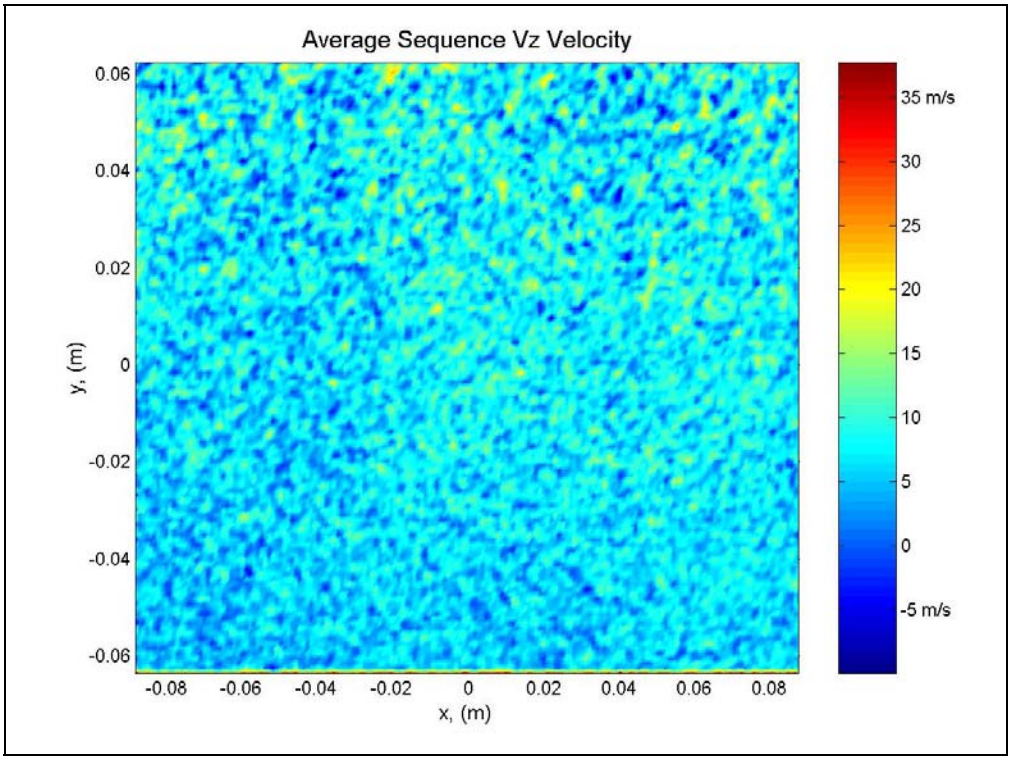

Figure 6.17: Contour plot of average z velocity components calculated by the image sequence data reduction procedure.

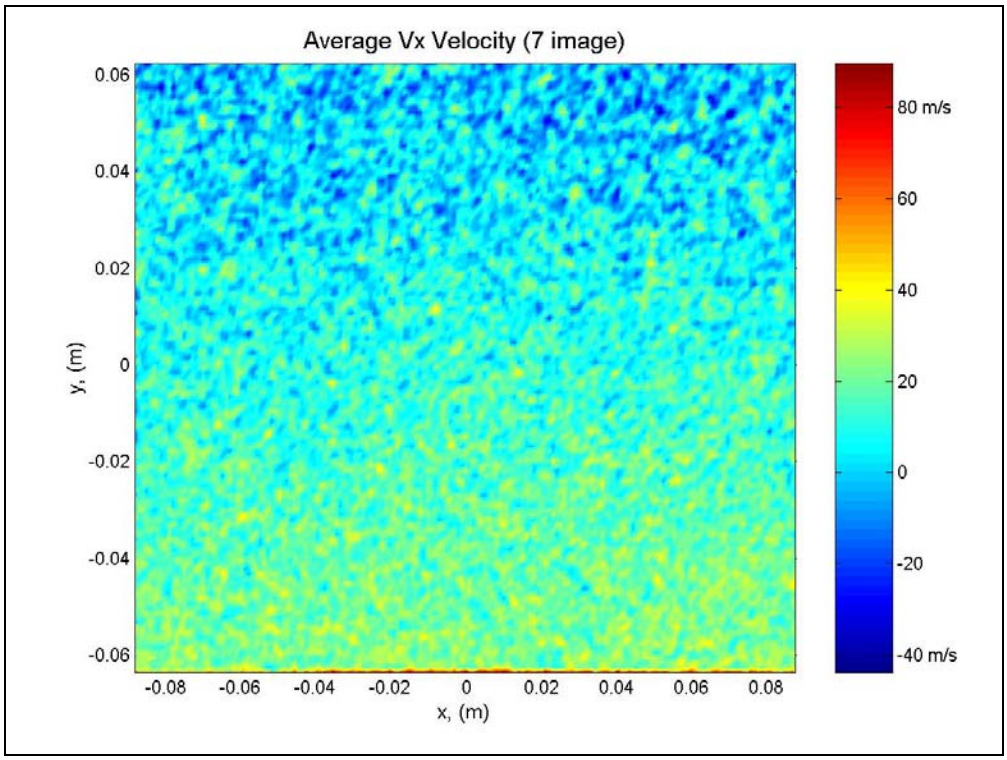

Figure 6.18: Contour plot of average x velocity components calculated from the average images.

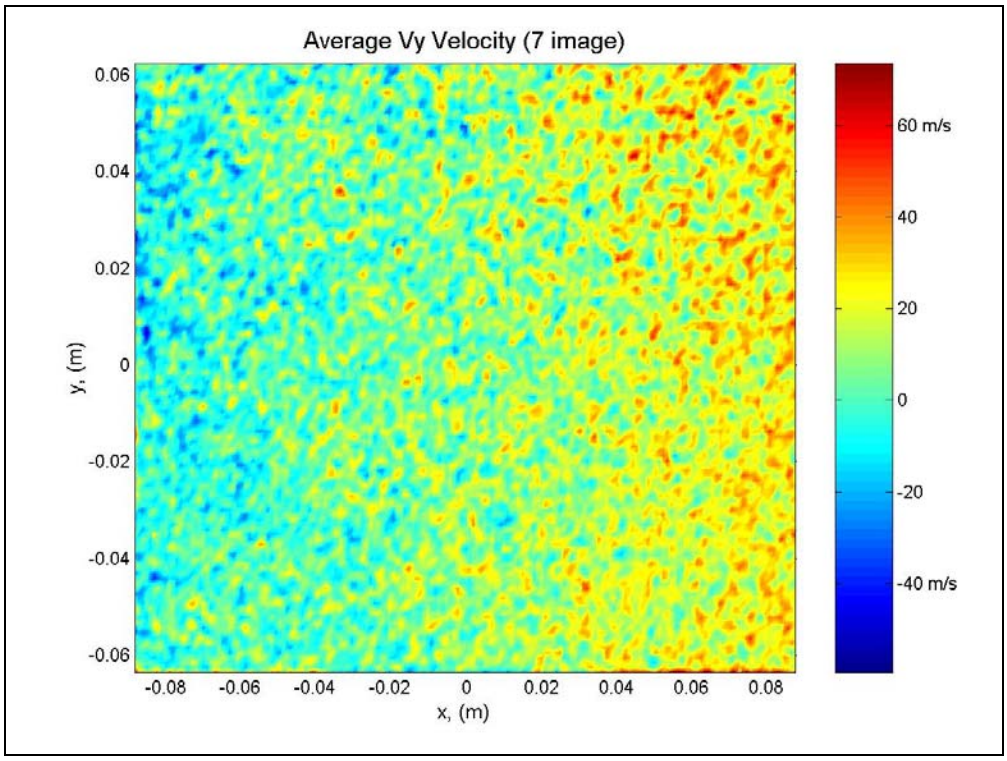

Figure 6.19: Contour plot of average y velocity components calculated from the average images.

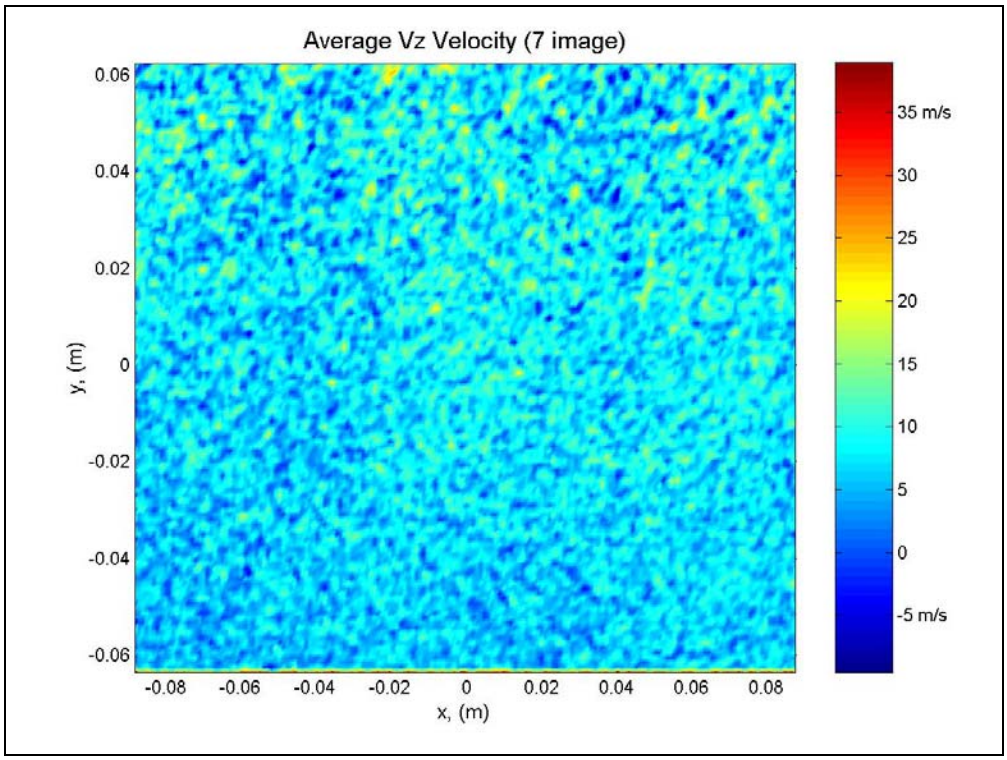

Figure 6.20: Contour plot of average z velocity components calculated from the average images.

Figures 6.21 and 6.22 show the x, y, and z velocity components along the horizontal and vertical centerlines of the calibration wheel, respectively, for the image sequence data reduction. Figures 6.23 and 6.24 show the x, y, and z velocity components along the horizontal and vertical centerlines of the calibration wheel, respectively, for the average image data reduction. These figures show that the magnitudes of the velocity components measured by the VT DGV system fluctuate considerably. There are several possible causes for these fluctuations. One possible cause for these fluctuations is spatial variations in optical frequency within each pulse used to illuminate the calibration wheel while the data image was acquired. These spatial variations could also be a contributing factor in explaining why the velocity components measured by the VT DGV system are significantly higher than the velocities calculated from the angular velocity of the wheel, but it is unlikely that these spatial variations are the major cause of this discrepancy. Another possible cause for the fluctuations in the velocity components measured by the VT DGV system is the roughness of the wheel surface. Sand paper was applied to the surface of the calibration wheel to facilitate light scattering, but it is possible the 400 grit sand paper applied to the surface was too coarse and causing shadowing to occur on the illuminated wheel surface.

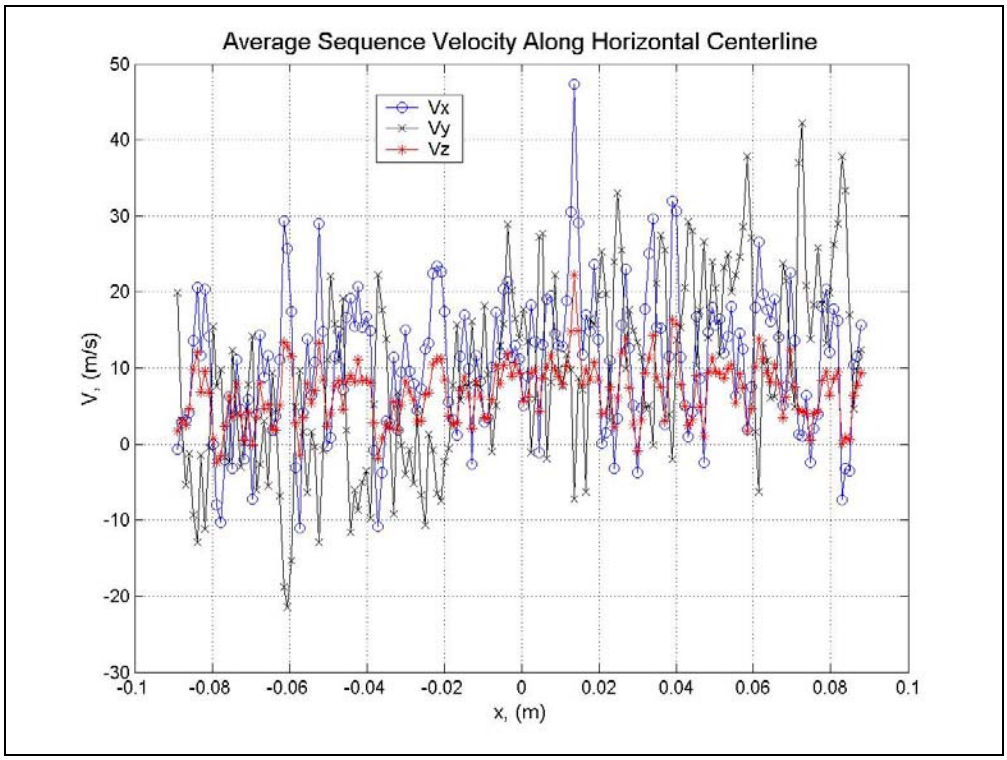

Figure 6.21: x, y, and z velocity components along the horizontal centerline of the calibration wheel, calculated during the image sequence data reduction.

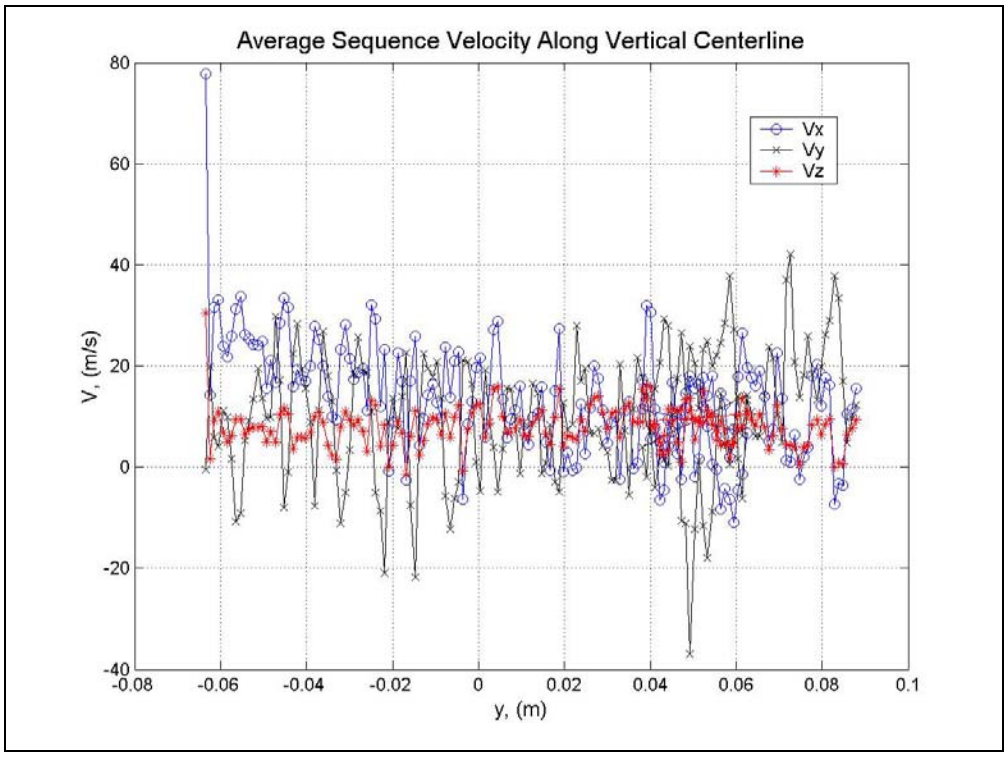

Figure 6.22: x, y, and z velocity components along the vertical centerline of the calibration wheel, calculated during the image sequence data reduction.

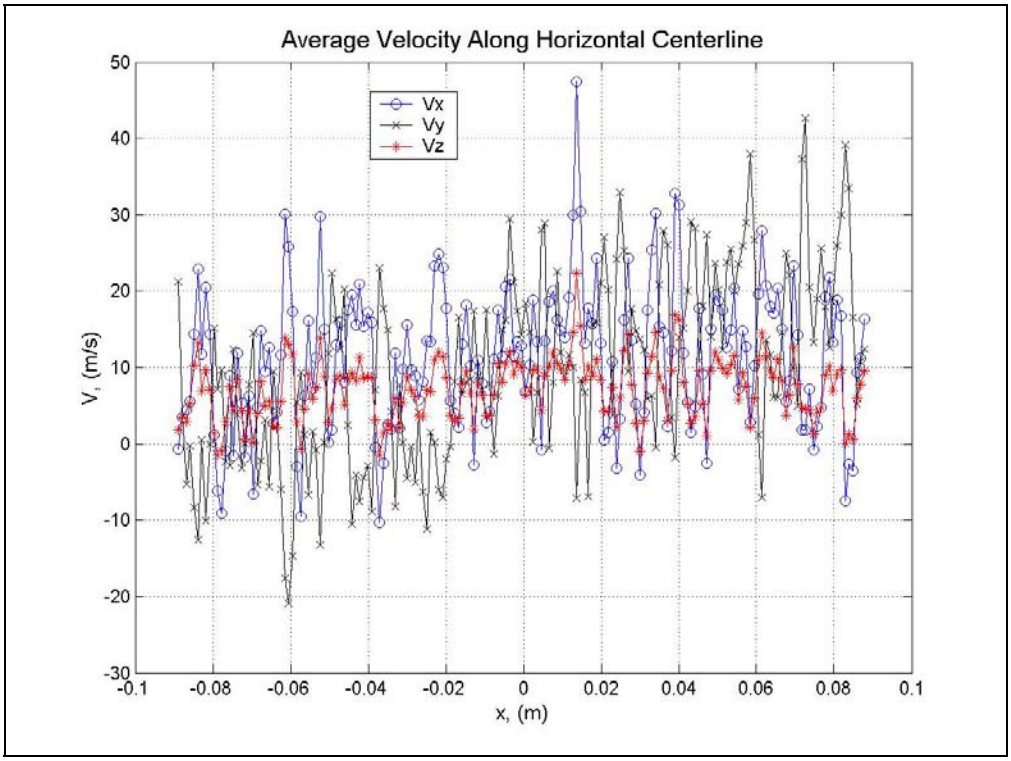

Figure 6.23: x, y, and z velocity components along the horizontal centerline of the calibration wheel, calculated during the average image data reduction.

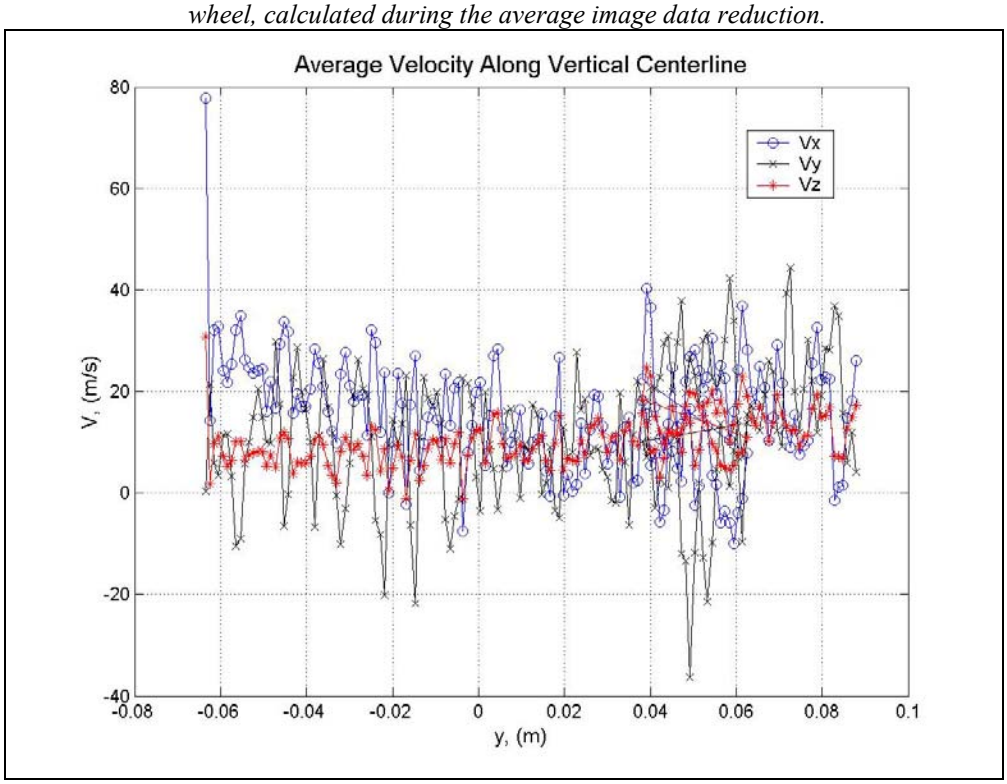

Figure 6.24: x, y, and z velocity components along the vertical centerline of the calibration wheel, calculated during the average image data reduction.

6.5.3 Individual Image Data Reduction

Because of the fluctuations observed in the results from the image sequence data reduction and the average image data reduction, and because only seven images were reduced in the image sequence data reduction and the same seven images were used to calculate the average images, each of the seven images was reduced individually. The contour plots containing the x, y, and z velocity components for each of the seven images can be found in Appendix A. Plots of the x, y, and z velocity components along the horizontal and vertical centerlines of the calibration wheel can be found in Appendix B. The contour plots and the plots of the velocity components along the vertical center line indicate that a small portion of the velocity data was lost in three of the seven images. The magnitude of the velocity components measured in these areas where data was lost was zero. The VT DGV data reduction program automatically assigns a value of zero for the transmission ratio at a particular pixel location if the pixel intensity in the reference view is zero. This prevents the program from trying to divide by zero when the transmission ratio is calculated. Also, if the transmission ratio input into the frequency calibration function is outside of the bounds set in the frequency calibration function dialog box, an optical frequency of zero is returned to the data reduction program. The data reduction program checks to see if the optical frequency is zero, if this is the case the change in optical frequency for the pixel is set to zero and hence the velocity calculated for the pixel will be zero. More than likely the problem with these images is that the transmission ratio for one of the three camera modules was outside of the maximum or minimum bounds set for calculating the optical frequency, in the region where data was lost. This theory is supported by the fact that there does not appear to be a problem with these images when they are viewed, but when they are reduced the velocities in a portion of the image are set to zero. If the pixel intensities in the reference view were zero for this region of the image it would be noticeable when the image was viewed. Because the results from these images were suspicious, another average image was calculated for each of the camera modules using the remaining four images. These new average images were reduced using the average image data reduction procedure. Figures 6.25, 6.26, and 6.27 are contour plots showing the x, y, and z velocity components for the new average images.

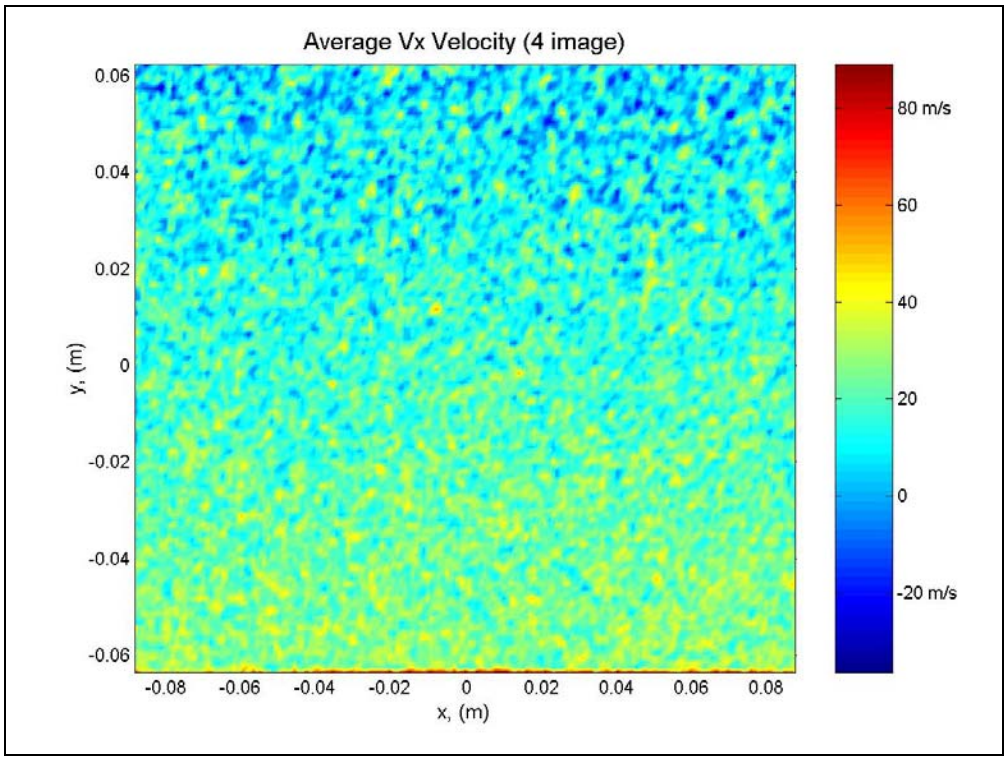

Figure 6.25: Contour plot of average x velocity components calculated from the new (4 image) average images.

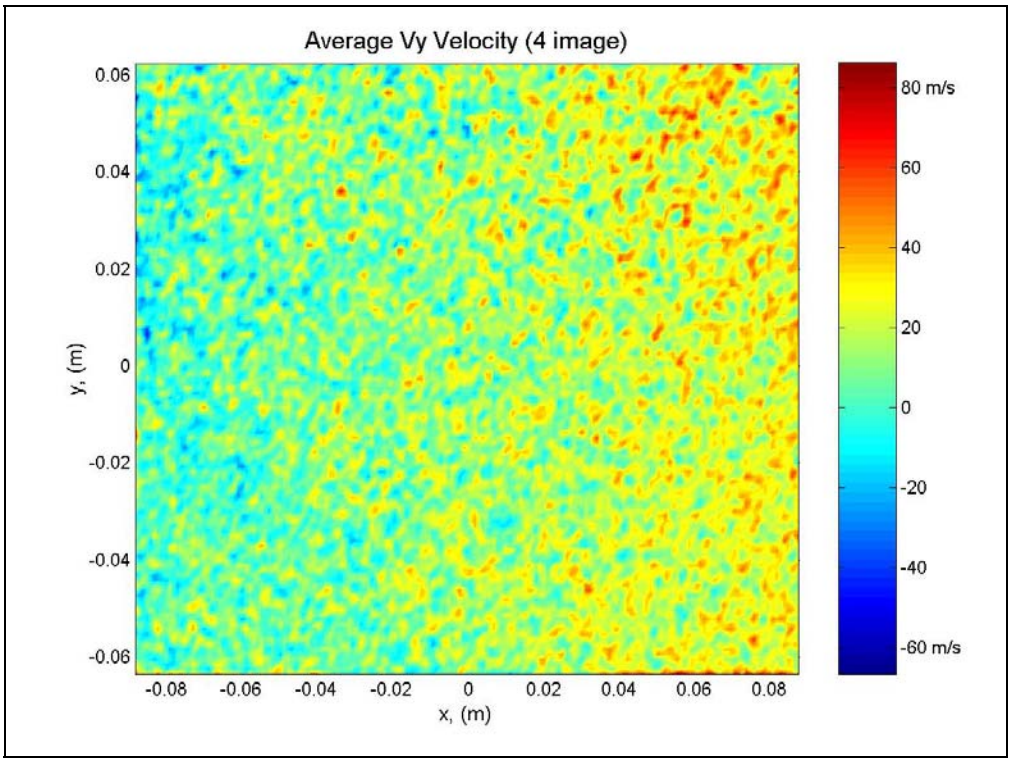

Figure 6.26: Contour plot of average y velocity components calculated from the new (4 image) average images.

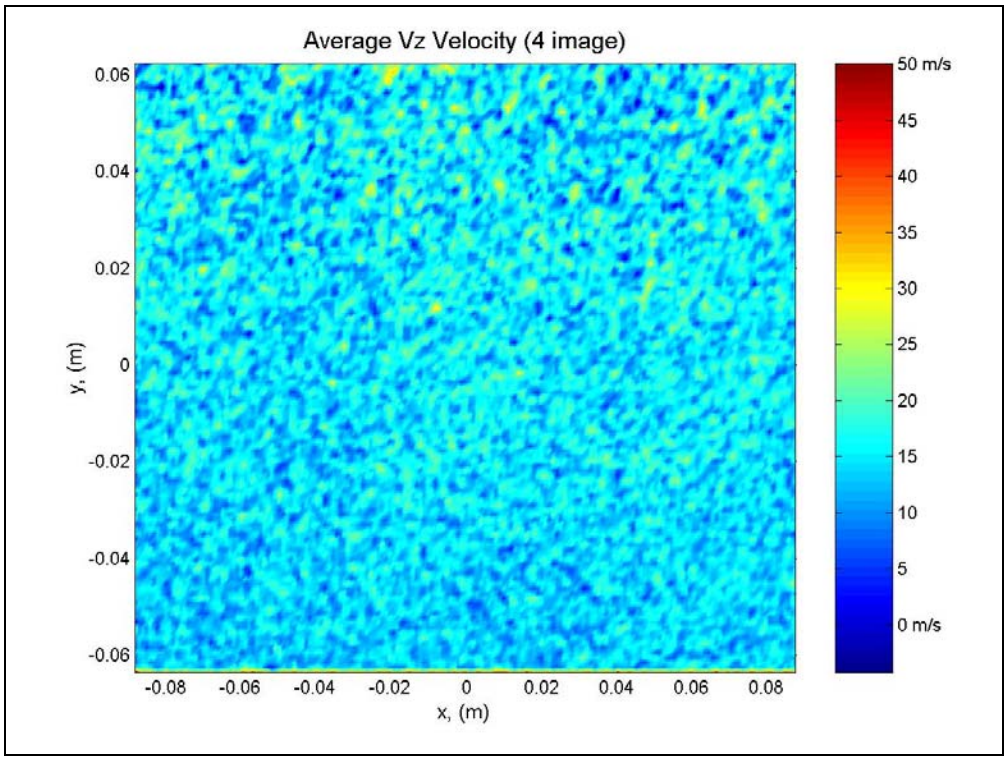

Figure 6.27: Contour plot of average z velocity components calculated from the new (4 image) average images.

Figures 6.28 and 6.29 are plots of the x velocity component along the horizontal and vertical centerlines, respectively, of the calibration wheel for the image sequence data reduction, seven image average image data reduction, four image average image data reduction and the values calculated using the seven image average angular velocity determined from the output voltage from the motor controller. Figures 6.30 and 6.31 are plots of the y velocity component along the horizontal and vertical centerlines, respectively, of the calibration wheel for the image sequence data reduction, seven image average image data reduction, four image average image data reduction and the values calculated using the seven image average angular velocity determined from the output voltage from the motor controller. Figures 6.32 and 6.33 are plots of the z velocity component along the horizontal and vertical centerlines, respectively, of the calibration wheel for the image sequence data reduction, seven image average image data reduction, four image average image data reduction and the values calculated using the seven image average angular velocity determined from the output voltage from the motor controller. Comparing the results from the three data reduction procedures, the velocities calculated by the image sequence data reduction and the seven image average data reduction closely agree, as expected. The magnitudes of the velocities calculated by the new, four image average data reduction are noticeably higher than those calculated using the other two data reduction procedures. As was indicated by the contour plots shown in figures 6.13 through 6.20, plots in figures 6.28

through 6.33 show the magnitudes of the velocities measured by the VT DGV system are generally much higher than those calculated using the angular velocity. Another important fact to note in these plots is that the plot of the x velocity component along the vertical centerline does appear to have the same trend shown in the velocities calculated from the angular velocity and the y velocity component along the horizontal centerline also appears to have the same trend shown in the velocities calculated from the angular velocity.

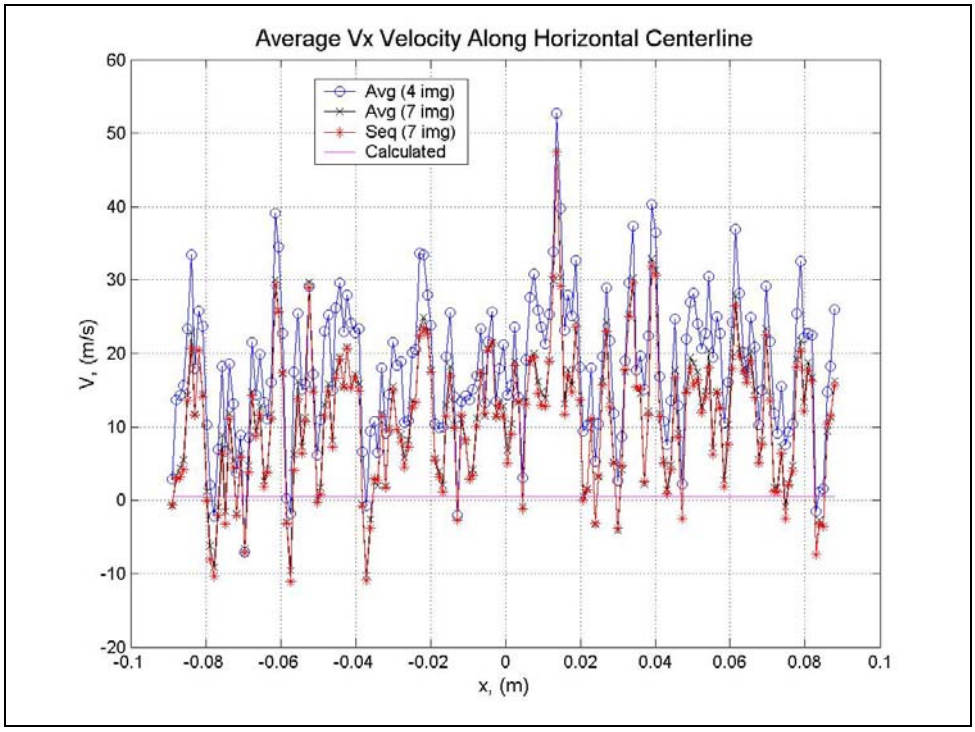

Figure 6.28: Plot of x velocity component along the horizontal centerline of the calibration wheel for the image sequence data reduction, average image data reduction, new (4 image) average image data reduction and the values calculated from the angular velocity.

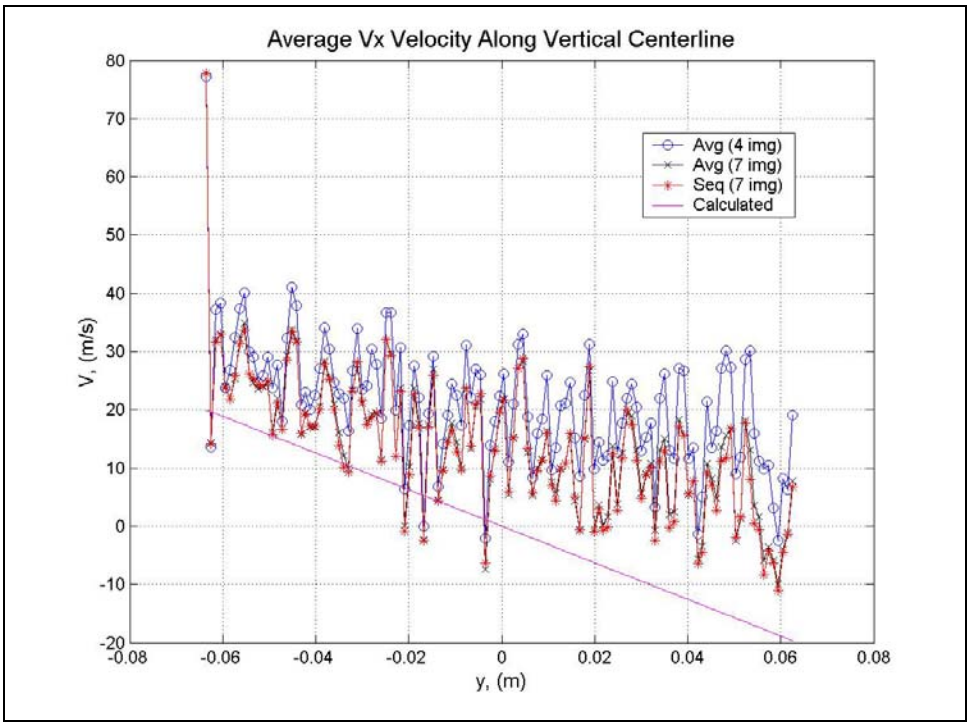

Figure 6.29: Plot of x velocity component along the vertical centerline of the calibration wheel for the image sequence data reduction, average image data reduction, new (4 image) average image data reduction and the values calculated from the angular velocity.

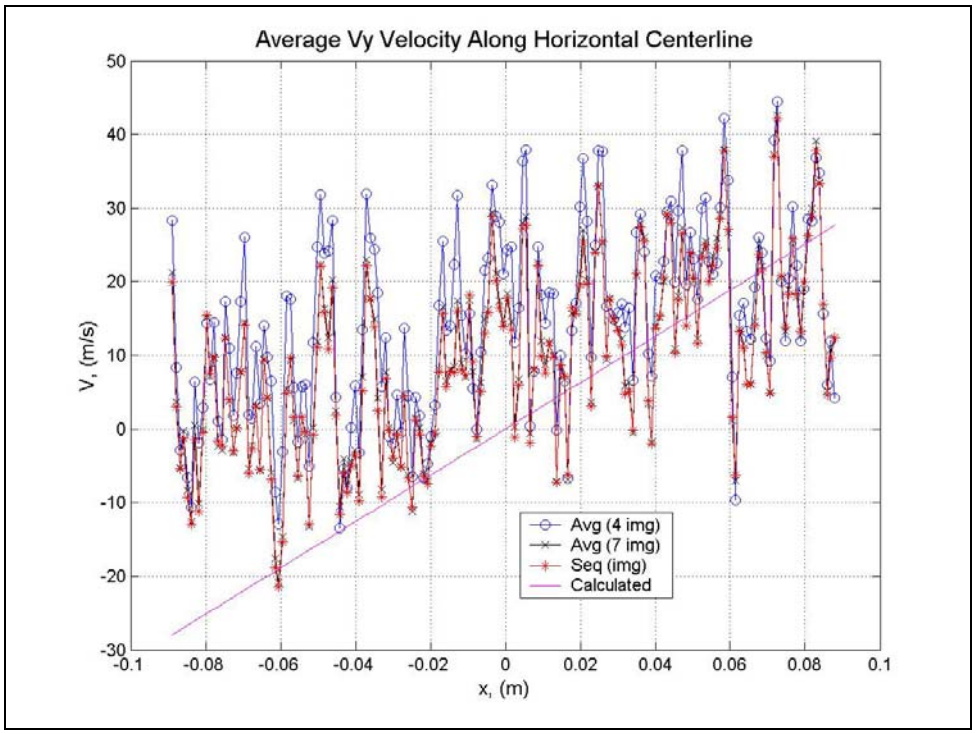

Figure 6.30: Plot of y velocity component along the horizontal centerline of the calibration wheel for the image sequence data reduction, average image data reduction, new (4 image) average image data reduction and the values calculated from the angular velocity.

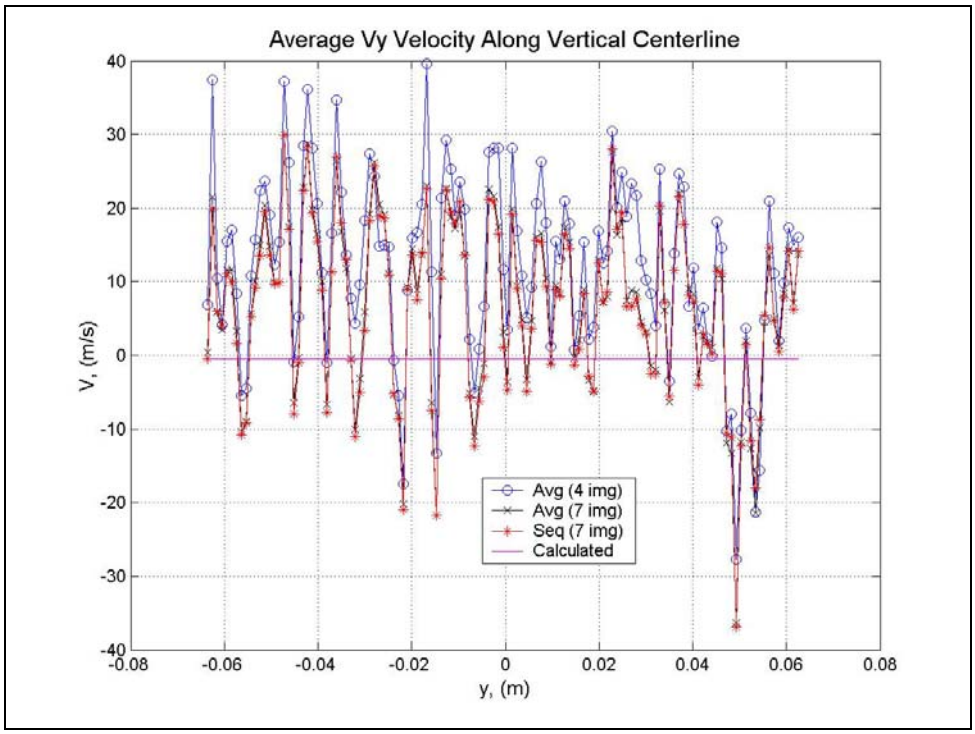

Figure 6.31: Plot of y velocity components along the vertical centerline of the calibration wheel for the image sequence data reduction, average image data reduction, new (4 image) average image data reduction and the values calculated from the angular velocity.

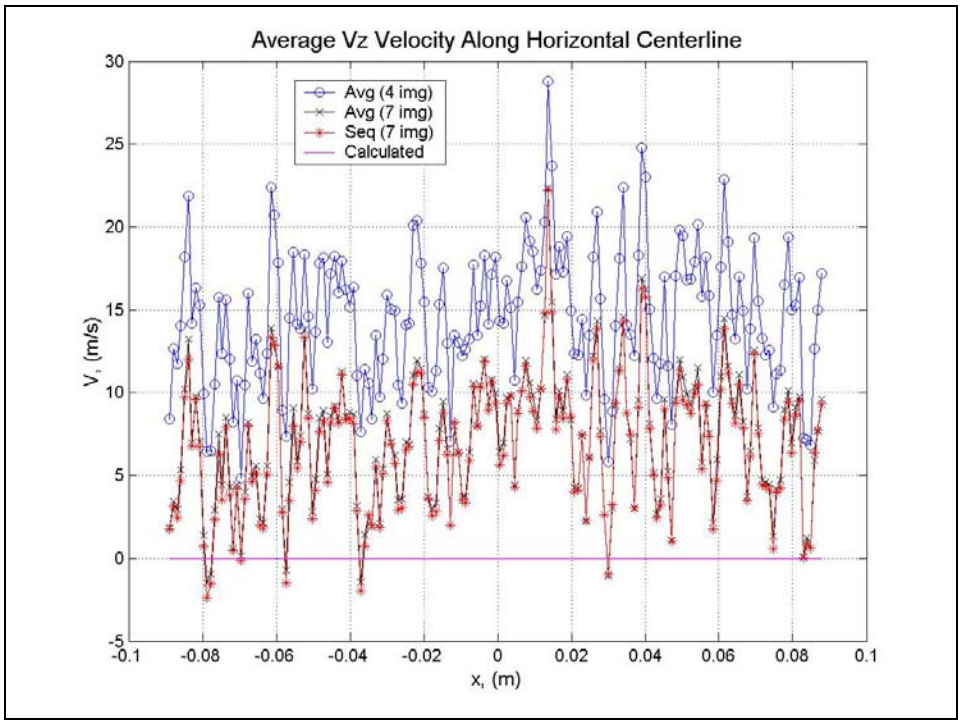

Figure 6.32: Plot of z velocity components along the horizontal centerline of the calibration wheel for the image sequence data reduction, average image data reduction, new (4 image) average image data reduction and the values calculated from the angular velocity.

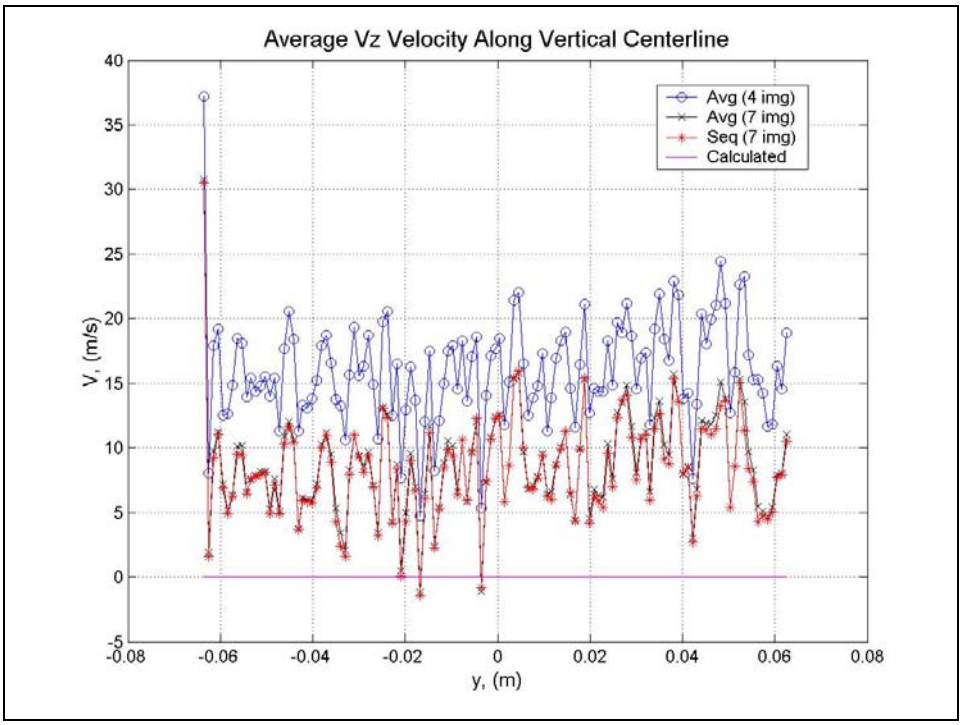

Figure 6.33: Plot of z velocity components along the vertical centerline of the calibration wheel for the image sequence data reduction, average image data reduction, new (4 image) average image data reduction and the values calculated from the angular velocity.

6.6 6:1 Prolate Spheroid Results

As was discussed in section 3.8, an attempt was made to acquire DGV data in the wake of a 6:1 prolate spheroid. The hardware problems discussed in Chapter 5 delayed this attempt until the last day of the wind tunnel entry. A full day was required to reposition the camera modules and set up the optics needed to form the laser sheet used to acquire DGV data in the flow field. Once the system setup had been adapted to acquire flow field data, four iodine cell calibrations were acquired before a usable calibration was found. Next, the correction images were acquired as described in section 3.8. Finally, the wind tunnel was started and the free stream velocity inside the test section was increased until a dynamic pressure of 4 inches of water was reached. Once the speed of the tunnel was set the smoke machine was enabled and seed particles were injected into the wind tunnel. A test image was acquired prior to an attempt to acquire a series of velocity data images. This test image did not show any measurable pattern of scattered light. The free stream velocity in the wind tunnel was decreased so the dynamic pressure was 3 inches of water and another test image was acquired. The results were the same as before, no measurable pattern of scattered light was captured by any of the camera modules. Another attempt was made at a dynamic pressure of 2.3 inches of water with the same results. This was the last attempt to be made because diffused smoke in the wind tunnel obscured the data plane. Figure 6.34 shows a false color version of one of the velocity data

images acquired by camera module 1, figure 6.35 shows a false color version of one of the data images acquired by camera module 2, and figure 6.36 shows a false color version of one of the data images acquired by camera module 3.

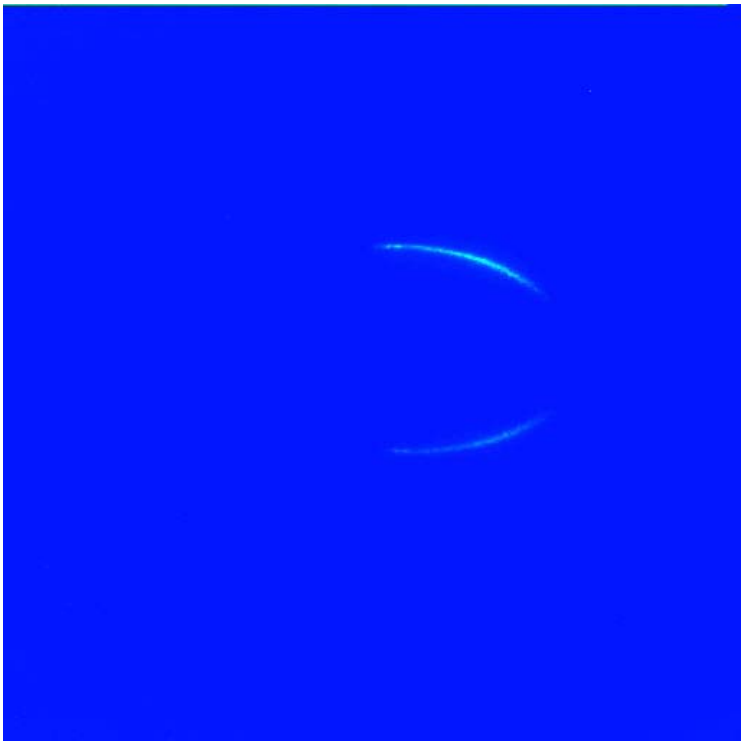

Figure 6.34: False color version of velocity data image acquired by camera module 1 of the flow in the wake of a 6:1 prolate spheroid model.

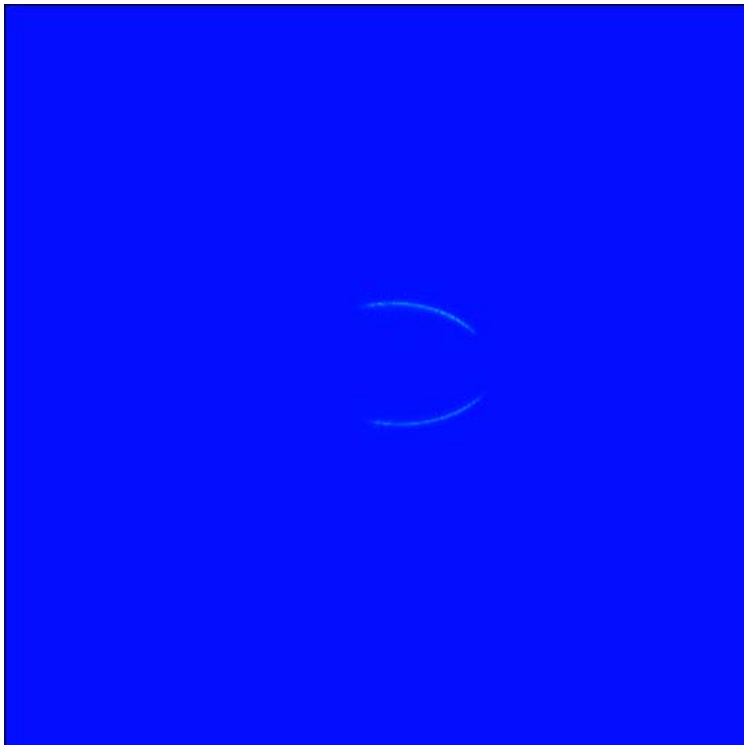

Figure 6.35: False color version of velocity data image acquired by camera module 2 of the flow in the wake of a 6:1 prolate spheroid model.

Figure 6.36: False color version of velocity data image acquired by camera module 3 of the flow in the wake of a 6:1 prolate spheroid model.

While the attempt itself was unsuccessful, some important lessons were learned. The first lesson learned is that an experiment with a flexible test schedule needs to be performed using the Nd:YAG laser, wind tunnel, smoke machine, model(s) to be tested, and one of the camera modules to try different smoke machine positions and injection methods to maximize the light scattering while minimizing the amount of smoke used. These tests would not necessarily need to be attempts to acquire DGV data. In fact, it would be advisable not to try to acquire DGV data in these attempts, but to only try to successfully acquire images of smoke particles passing through the laser sheet. This would significantly simplify the test schedule and decrease the number of tasks to be performed between attempts. The smoke machine filled the wind tunnel with smoke in a very short period of time (roughly 5 minutes) so the smoke machine appears to be capable of producing enough smoke to acquire DGV velocity images. The stream tube containing the smoke plume may have been too large and was most likely in the wrong location to acquire velocity images in the wake of the prolate spheroid. Another important lesson was that skilled and attentive help is needed when flow velocity data are to be acquired with the VT DGV system. The people who assisted with setting up the VT DGV system during this research were smart, skilled, and attentive people, but these people were not present when the attempts to acquire velocity data in the wake of the prolate spheroid were made. The VT DGV system requires at least two skilled people to acquire flow velocity images. One of these people would run the DGV control computer and acquire the images and the other person would be responsible for running the wind tunnel and smoke machine. The second person would have to pay close attention to the size and location of the smoke plume and make the person running the DGV control computer aware of any problems encountered. A third experienced person would also prove very helpful in monitoring the performance of the Nd:YAG laser until confidence in the performance of the laser is gained.

6.7 General Comments

While the performance of the VT DGV system was less than expected, some valuable lessons have been learned. Considerable time was needed to set up the VT DGV system in the wind tunnel. Future work on the system needs to address this problem by making the system easier to setup, reposition, and take down as well as addressing the hardware problems within the system. A permanent laser optics setup needs to be designed and constructed. In the previous tests of the VT DGV system as well as the tests performed in this research the laser optics were temporarily set up on a pair of optical tables. The first table was where the laser was placed and the optics on this table were used to fire the laser into the control room. The second table held the optics used to create the cone of laser light and the laser sheet. Precious time was needed to set up and adjust the laser optics.

A compact and permanent setup would save set up time and potentially eliminate some of the frequent adjustments needed during this research. Every effort was made to eliminate stray reflections from the laser optics. Covers were designed and constructed to cover the optics and eliminate these reflections. This was done for two reasons, to make the area where the system was being used safer and to also try to eliminate possible sources of "noise" in the system since the light from these stray reflections could easily be acquired by the camera modules. The background correction images may or may not be able to account for all of these stray reflections, depending on how the correction images were acquired. Special windows made of optical quality glass are needed where the laser is being fired into the test section as well as where the camera modules are placed to view the data plane. Scratches and imperfections in the Plexiglas windows degraded the uniformity in the illumination of the data area and the quality of the images acquired by the camera modules. Holes were cut into the Plexiglas panels where the laser was to pass through to prevent the laser from burning the panel and to allow the data area to be illuminated as uniformly as possible. The windows to be made for the laser to pass through will need to be made of a material capable of surviving the high power output from the laser. Also, the hardware problems with the system must be addressed aggressively. The problems with the stability of the Nd:YAG laser coupled with the problems with the digital cameras severely hampered the progress of this research and ultimately led to the poor performance of the system during the attempts to acquire velocity images. The hope of future success with the VT DGV system rests on permanently solving these hardware problems. A way must be found to stabilize the performance of the Nd:YAG laser and to make it more reliable or the laser must be replaced with a another laser, possibly another type of laser. An argon ion laser may, in fact, be a possible alternative to the Nd:YAG laser. The digital camera with the problem of forming ice crystals must be replaced. Using the system an hour at a time was not only inconvenient, it prevented this research from progressing in a timely manner and prevented other problems with the system from being diagnosed and fixed. In addition to the work described above, much work remains to be done before the system can be used in conjunction with the Dynamic Plunge Pitch and Roll (DyPPiR) apparatus. Finally, the modifications suggested in the paper published by Meyers *et al,* in 2001 and discussed in Chapter 1, need to be reviewed and where possible implemented to improve the performance of the VT DGV system. In particular, the modification needed to monitor spatial variations in the optical frequency from pulse to pulse should be implemented as soon as it is practical.[106]

Chapter 7: Uncertainty Analysis